

UC Berkeley

UC Berkeley Electronic Theses and Dissertations

Title

Anisotropic and Negative Acoustic Index Metamaterials

Permalink

<https://escholarship.org/uc/item/21h3j5xr>

Author

Fok, Lee Ren

Publication Date

2010

Peer reviewed|Thesis/dissertation

Anisotropic and Negative Acoustic Index Metamaterials

By

Lee Ren Fok

A dissertation submitted in partial satisfaction of the

requirements for the degree of

Doctor of Philosophy

in

Engineering – Mechanical Engineering

in the

Graduate Division

of the

University of California, Berkeley

Committee in charge:

Professor Xiang Zhang, Chair

Professor David B. Bogy

Professor Ture K. Gustafson

Fall 2010

Anisotropic and Negative Acoustic Index Metamaterials

© 2010

Lee Ren Fok

Abstract

Anisotropic and Negative Acoustic Index Metamaterials

by

Lee Ren Fok

Doctor of Philosophy in Engineering – Mechanical Engineering

University of California, Berkeley

Professor Xiang Zhang, Chair

Microstructured materials are used in material science and engineering to attain desired material properties. Acoustic metamaterials are a rapidly growing area in this field of engineered materials that use deep subwavelength microstructures to attain exotic acoustic properties unavailable in nature. These properties, such as negative acoustic index, allow unprecedented capabilities such as sub-diffraction limit resolution, which have the potential to greatly improve existing technologies like high intensity focused ultrasound, sound shielding, and ultrasonic imaging, as well as create the entirely new ones like acoustic cloaking and energy trapping. Two acoustic material properties were pursued in this dissertation, anisotropic density and negative acoustic index.

Anisotropic density in a fluid acoustic metamaterial was pursued for use in a 2D acoustic hyperlens. Originally developed to image sub-diffraction limit electromagnetic information in the far-field, the theory behind the hyperlens imaging method in acoustics is presented and the performance is shown to be directly related to the density anisotropy magnitude. An acoustic metamaterial composed of alternating deep subwavelength layers of air and brass is then shown theoretically and numerically to attain the necessary density anisotropy, with a three order of magnitude difference in component amplitudes. Experiments using a 2D cylindrical acoustic hyperlens constructed from this metamaterial confirm a significant portion of the evanescent components are converted into propagating components at the lens exit, resulting in far-field acoustic imaging of information far below the diffraction limit.

Development of a negative acoustic index fluid metamaterial was motivated by the reversed wave phenomena leading to a perfect lens. Negative bulk modulus and density are shown in simulations to result from the combination of Helmholtz and rod-spring resonators, which creates a band in the power ultrasound frequency range with negative real acoustic index components. Following a several design changes to accommodate the available experimental facilities, samples of this metamaterial were tested and indeed found to attain a negative real component of acoustic index. However, intrinsic loss and design restrictions led to a small real to imaginary index component ratio, severely limiting the application prospects of this metamaterial. Work on active acoustic metamaterials to overcome these and other problems follows, with simulations indicating piezoelectric elements in water may be used as gain elements to amplify damped waves or as direct replacements for passive resonators that both combat loss and broaden the bandwidth of anomalous properties.

Table of Contents

List of Figures	iii
List of Tables	vi
List of Symbols	vii
Chapter 1 – Introduction	
Metamaterials Background	1
Dynamic Acoustic Material Properties	2
Acoustic – EM Comparison	4
Effective Medium Theory	5
Historical Engineered Acoustic Materials	6
Metamaterial Approaches and Dissertation Outline	7
Chapter 2 – Anisotropic Acoustic Metamaterials for Hyperlens	
Introduction	9
Hyperlens Theory	9
Anisotropic Acoustic Metamaterial Design	12
Shear Mode Coupling	15
Summary	16
Chapter 3 – Acoustic Hyperlens Experiments	
Introduction	17
Acoustic Hyperlens Design and Experimental Setup	17
Experimental Results	18
Internal Hyperlens Fields	21
Future Directions	23
Summary	26
Chapter 4 – Negative Acoustic Index Metamaterials	
Introduction	27
Negative Acoustic Index Physics and Metamaterial Design	28
Negative Acoustic Index Metamaterial Simulations	31
Summary	34
Chapter 5 – Negative Acoustic Index Metamaterial Experiments	
Introduction	35
Waveguide Setup Testing	35
Experimental Negative Acoustic Index Metamaterial Design and Setup	36
Experiment Results and Discussion	39
Future Directions	42
Summary	45

Chapter 6 – Active Acoustic Metamaterials

Introduction	46
3D Acoustic Hyperlens	46
3D Negative Acoustic Index Resonators	47
Active Acoustic Metamaterial Background	49
Active Acoustic Metamaterial Investigations	51
Summary	54

Chapter 7 – Conclusions and Outlook

Conclusions	56
Outlook	56

References	58
-------------------	-----------

List of Figures

Figure 1.1 Effective medium approximation: microstructure details much smaller than the wavelength can be replaced with homogenous properties. _____ 2

Figure 2.1 Possible equi-frequency contours in a 2D anisotropic acoustic metamaterial. The red line denotes isotropic density, the blue line denotes anisotropic density with positive density components, and the black line denotes anisotropic density with negative ρ_y . In both anisotropic cases, ρ_y is greater in magnitude than ρ_x . _____ 10

Figure 2.2 Imaging using flat dispersion lenses in (Left) rectangular Cartesian coordinates, and (Right) cylindrical coordinates. _____ 12

Figure 2.3 Simulation of metamaterial formed from alternating layers of brass (white) and air (color) to extract x-direction properties. The x-direction is parallel and y-direction perpendicular to a brass layer. The air regions beyond the brass layers are the ends of waveguides used in the simulation. _____ 12

Figure 2.4 Extracted (Left) bulk modulus and (Right) mass density of the air/brass metamaterial in the x-direction. Real components are plotted in magenta and imaginary in black. _____ 14

Figure 2.5 Extracted (Left) bulk modulus and (Right) mass density of the air/brass metamaterial in the y-direction. Real components are plotted in magenta and imaginary in black. _____ 14

Figure 2.6 Fraction of energy coupled to the brass pure shear mode from the input plane wave in air at the interface between half-spaces. _____ 16

Figure 3.1 Acoustic hyperlens used in experiments with the cover sheet removed. _____ 17

Figure 3.2 Two source hyperlens results. (Left) Experimental acoustic hyperlens with pressure field measurements superimposed. (Right) Simulated acoustic hyperlens pressure field using the analytically determined effective properties. _____ 19

Figure 3.3 Verification of hyperlens effects at 6.6 kHz. (Left) Comparison of pressure amplitude along an arc just beyond hyperlens outer radius with the hyperlens in red and without the hyperlens in blue. (Right) Phase and amplitude measurements, in red and blue respectively, along a beam exiting the hyperlens. The marks are experimental data and the lines are values predicted from simulation. _____ 19

Figure 3.4 Broadband hyperlens performance. The amplitude at each frequency has been normalized to allow plotting on the same figure. _____ 20

Figure 3.5 Hyperlens imaging of three speaker source. (a) Experimental results superimposed on hyperlens, (b) 2D simulation of three speaker setup with high pressure amplitudes inside hyperlens saturated to white, (c) Trio of speakers used in experiment. _____ 21

Figure 3.6 Pressure field at hyperlens midplane from 3D simulation of experimental hyperlens. Brass fins are white while pressure field is plotted in color representing local pressure value, with strong pressure values in the inner hyperlens washed out to white as well. _____ 22

Figure 3.7 Brass and air acceleration components in the (Left) radial direction and (Right) angular direction. The brass acceleration is plotted in rainbow color scale and the air vibrations in gray scale. The color bar and gray scale bar limits (units: m/s^2) in the radial case are $\pm 3 \times 10^{-4}$ and ± 300 respectively, and the analogous limits in the angular case are $\pm 2 \times 10^{-3}$ and ± 75 . ____ 23

Figure 3.8 Effect of fin periodicities larger than allowed by the effective medium approximation. (Left) Effective medium simulation, (Right) simulation with fin periodicity larger than a wavelength at the exit. _____ 24

Figure 3.9 Cascaded hyperlens design allowing increased magnification via increased outer radius. _____ 24

Figure 3.10 Water filled flat hyperlens with phase correction addition using (Left) rigid walls and (Right) elastic brass walls. _____ 25

Figure 4.1 Negative acoustic index metamaterial design. (Left) Unit cell consisting of RS resonator in red and four HH resonators in blue, (Right) RS resonator consisting of aluminum mass in red connected to PMMA springs in blue. _____ 29

Figure 4.2 Simulation domain with negative index unit cell in center. Plane waves travel from the bottom left boundary towards the top right boundary. _____ 32

Figure 4.3 Effective refractive index of the negative acoustic index metamaterial unit cell from simulations. _____ 33

Figure 4.4 Effective (Left) bulk modulus and (Right) density of the negative acoustic index unit cell from simulations. _____ 33

Figure 5.1 Aluminum waveguide pulse experiment results. (Left) Oscilloscope trace of input signal in orange and hydrophone signal in teal at 25 kHz. The first received pulse is the hybrid mode and the second the water mode. (Right) Phase speed of water mode inside the waveguide. _____ 35

Figure 5.2 Negative acoustic index metamaterial sample. Rods from the RS resonator and the neck openings of HH resonators are visible. _____ 36

Figure 5.3 Experimental test bay with roof removed. The spherical source and heater can be seen on the left, lens left of center, sample right of center, and receiver on the right of the sample. A rail frame constructed from stainless steel rods and blocks of SADM-1 was used to position the receiving hydrophone in a repeatable manner. _____ 37

Figure 5.4 Transmission coefficient amplitudes of a control sample. Thin lines denote measurements with the sample at different positions in the cavity, while the thick line is the average of the thin lines. _____ 39

Figure 5.5 Effective acoustic index of best performing experimental negative acoustic index sample. _____ 40

Figure 5.6 Effective (Left) bulk modulus and (Right) density of the best performing experimental negative acoustic index sample. _____ 40

Figure 5.7 Top view of the simulated 2D negative acoustic index metamaterial composed of membrane and side-hole resonators. The source beam enters the domain via the bottom left 30° angled boundary. The inner circle outlines the boundary of a smaller hemisphere serving as open air, while the outer circle is the boundary of the hemispherical absorbing shell. _____ 42

Figure 5.8 Effective bulk modulus (left) and density (right) of metamaterials composed of membranes alone (red), HH resonators alone (green), and the combination (blue). _____ 43

Figure 5.9 Alternative membrane resonator designs. (Left) Membrane with corner cutouts, and (Right) membrane with large square cross-section mass in center and corner cutouts. _____ 44

Figure 5.10 New negative density resonator. (Left) Simulation of unit cell with deformed shape plotted in color. (Right) Effective density as a function of frequency for various polymer fin loss levels. The Re and Im refer to the real and imaginary density components, and the percentage to the loss factor magnitude _____ 44

Figure 6.1 3D spherical hyperlens. (Left) Solid model of hyperlens created in Solidworks®, (Right) Comsol® simulation at 5 kHz showing magnification of $\lambda/5.7$ disc speakers. _____ 46

Figure 6.2 3D negative density resonator. (Left) Simulation unit cell with displacement plotted in color slices. (Right) Effective density as a function of frequency for various loss factors. ____ 48

Figure 6.3 Rotated 3D negative density resonator. (Left) Simulation unit cell with displacement plotted in color slices. (Right) Effective density for various loss factor amounts. _____ 48

Figure 6.4 Pressure field snapshot of active acoustic metamaterial unit composed of a water core and two symmetric flush mounted piezoelectric elements (white rectangles) sandwiched between water filled waveguides. _____ 50

Figure 6.5 Effective acoustic index of the active acoustic gain metamaterial with piezoelectric elements driven at 0.01V acting on a 1 Pa incoming wave. _____ 51

Figure 6.6 Effective (Left) bulk modulus and (Right) density of the active acoustic metamaterial unit cell driven at 0.01 V with various phases relative to the incident wave. Real components are plotted in black and imaginary components in red. _____ 53

Figure 6.7 Effective bulk modulus of the active acoustic metamaterial unit cell for (Left) zero phase and increasing driving voltages and (Right) constant 0.2 V amplitude and $\pi/8$ phase shifts from zero phase. Real components are in black and imaginary components in red. _____ 54

List of tables

Table 2.1 Hyperlens Material Properties _____	13
Table 4.1 Negative Acoustic Index Material Properties _____	32

List of Symbols

ε	electric permittivity
λ	wavelength
μ	magnetic permeability
ν	Poisson ratio
ρ	density
ω	angular frequency
B	bulk modulus
E	energy flux
EM	electromagnetic
F	force
H	magnetic field
HH	Helmholtz
L'	Helmholtz resonator effective neck length
PZT	lead-zirconate-titanate
RS	rod-spring
RT	reflection and transmission
S	Helmholtz resonator neck cross-section area
S_E	elastic compliance
T	transmission coefficient
V	volume
Y	Young's modulus
a	acceleration
c	phase speed
d	piezoelectric charge constant
f	volume filling fraction

g	gravitational acceleration
h	height
k	wavevector
m	element mass
n	refractive index
p	gauge pressure
z	impedance

Chapter 1 – Introduction

Metamaterials Background

Material properties in acoustic and elastic wave theory include elastic constants and density and define the average response of materials to applied forces. Traditionally, these properties are defined as the static value, determined using equilibrium measurements such as weighing an object to determine density. Acoustic and elastic properties of naturally available materials are limited to positive real values. Imaginary components are neglected or considered separately as loss coefficients. However, within these constraints the available range of acoustic and elastic materials properties is vast, from low density, highly compressible gases to virtually incompressible heavy metals.

In spite of this selection, much work in mechanical engineering and material science focuses on creating acoustic and elastic materials with properties outside those available in nature for improved strength, weight, economy, or other engineering purpose. New materials have been created by combining basic materials into a homogenous mixture, such as metal alloys, distinct multi-component systems like reinforced concrete, and complex combinations of both such as carbon fiber. The resultant engineering developments from the increased property availability have been revolutionary in improved performance and decreased cost. However, the resultant properties are still typically confined to the traditional single, positive, real value within frequency ranges of interest.

The goal in this work was to create novel new materials with properties completely outside these traditional boundaries in pursuit of new physical phenomena and applications. Metamaterials offer a paradigm to such unique material properties. Originally conceived in the field of electromagnetic (EM) materials, with the term coined by Smith¹, the field of metamaterials utilizes the macroscopic nature of material properties, which in EM are electric permittivity ϵ and magnetic permeability μ . Instead of focusing on complex microscopic details such as individual electron-core interactions and defects, ϵ and μ describe the average resultant electric or magnetic field caused by an applied field of the same type for a sufficiently large sample².

Metamaterials seize on this averaging, or homogenization, by replacing naturally occurring microstructures with very small engineered unit cells capable of strong effects. Referring to Figure 1.1, provided the wavelength λ is sufficiently long relative to the engineered unit cell center-to-center spacing a , effective medium theory can still be applied and material properties assigned. The first design created under the EM metamaterial label, split ring resonators and wires, was a combination of previously reported microstructured materials shown to cause negative effective ϵ or μ individually. Combining these resonators in the same metamaterial resulted in the first experimentally demonstrated negative index material, with negative EM refractive index over a band in the microwave frequency range. Many EM metamaterial designs for negative index and related applications have been subsequently proposed and demonstrated, with applications ranging from cloaking³ to photonic circuit components⁴.

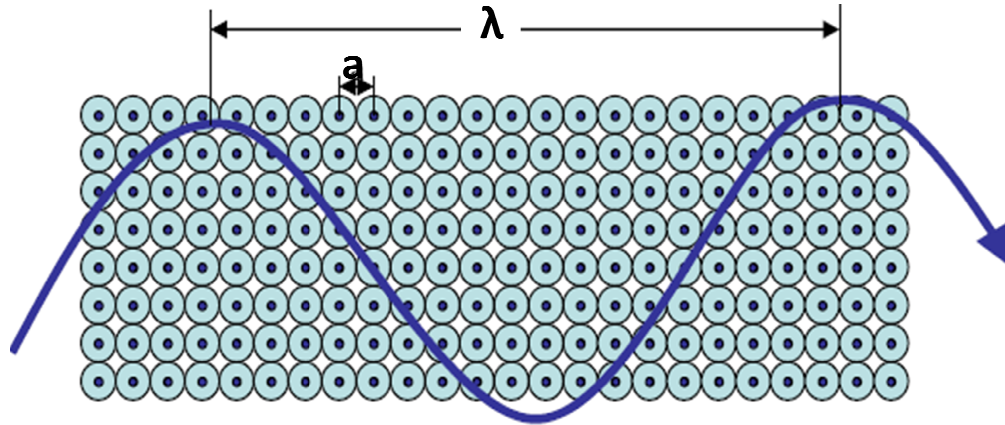


Figure 1.1 Effective medium approximation: microstructure details much smaller than the wavelength can be replaced with homogenous properties.

Analogous to their electromagnetic counterparts, acoustic and elastic properties are also defined through effective medium theory, taking an average value and ignoring the detailed microscopic interactions. For example, density is normally defined as the mass in a given volume divided by that volume. This is only well defined when the volume is much larger than defects and grain boundaries, when microscopic details are blurred out and a stable average value independent of position is obtained. This macroscopic nature of acoustic properties should make it possible to create acoustic metamaterials both analogous to those in EM and with characteristics unique to acoustics.

Many potential new phenomena and applications are possible using acoustic metamaterials. The ability to create arbitrary position dependent acoustic properties would open the door to applications from transformation mathematics such as cloaking objects from sound and trapping or focusing acoustic energy for extraction or chemical/biological reaction purposes. Anisotropic acoustic properties would add another dimension to fluid acoustic materials, allowing highly unusual dispersions and the associated novel effects. Negative refractive index in acoustics, as in EM, would permit imaging and focusing beyond the diffraction limit, improving non-destructive testing and medical ultrasound resolution. These negative properties in acoustics would also change common assumptions when solving for propagating modes at interfaces and in layers, leading to new waves and other unusual behaviors.

Dynamic Acoustic Material Properties

The work presented here was focused specifically on creating metamaterial fluids with novel dynamic effective properties. The dynamic aspect of these properties refers to the response of a material to harmonically oscillating excitation instead of static or quasi-static forces. In making this change, the definition of the relevant properties must be made explicit. For fluids, these properties are density and bulk modulus, with the shear modulus assumed to be zero. This assumption is valid provided the metamaterial does not support shear waves or the shear

modes do not couple or contribute to the motions of interest. Effects of this assumption being invalid are noted in the following definitions.

Bulk modulus B is a scalar property relating the volumetric change of a material to isotropic applied pressure. The standard definition is given in Equation 1.1.

$$B = -V \frac{\partial p}{\partial V} \quad (1.1)$$

In Equation 1.1, V is the element volume and p is the gauge pressure applied to the element. The minus sign is included so positive bulk modulus describes decreased volume from a compressive force, which is the natural behavior that always occurs in the static limit for real materials for stability reasons. When the applied pressure is harmonically oscillating, pressure and volume become complex numbers, resulting in a complex bulk modulus in which the phase describes the lag between pressure and volume change.

In the event a material supports transverse, longitudinal, and mixed modes, it is necessary to utilize additional elastic constants beyond bulk modulus, which by definition remains the same. The number of independent constants can range from two for homogenous isotropic media to an infinite number of constants for non-linear coupled materials. However, these all will have the same form as Equation 1.1, with the property relating a stress to a strain.

The definition of density for acoustic metamaterials is given in Equation 1.2, which is a form of Newton's second law.

$$\vec{\rho}_{dynamic} = \frac{1}{V} \frac{\vec{F}}{a} \quad (1.2)$$

In Equation 1.2, ρ is the density, a is the acceleration, and F is the total force applied to the media. Arrows over a term indicate the value is a vector instead of a scalar, which for density is necessary since force and acceleration are vectors. As with bulk modulus, when force and acceleration are time harmonic, density becomes complex with a phase that represents the lag between the applied force and resultant acceleration. This more complex definition of density is necessary for dynamic oscillating systems in which strong local interactions far below the wavelength cause density to deviate from the volume averaged value. An explanation of the necessity and physical background of this equation can be found in numerous sources; one is a recent in-depth paper by Milton and Willis⁵ and the references contained within. Of course, the static definition of density can be recovered from Equation 1.2 by defining the force as the gravitational force (mass m times gravity g) and the acceleration as g , which results in Equation 1.3.

$$\rho_{static} = \frac{m}{V} \quad (1.3)$$

Acoustic – EM Comparison

Given the advanced state of development in EM metamaterials relative to acoustic metamaterials, the similarities and differences between acoustics and electromagnetism are examined to understand which EM developments may in principle be transferred directly. Mathematically, the governing differential equations for EM and acoustic waves can be written in the same form as shown in Equations 1.4 and 1.5.

$$\left(\frac{\partial}{\partial x} \frac{1}{\varepsilon_y} \frac{\partial}{\partial x} + \frac{\partial}{\partial y} \frac{1}{\varepsilon_x} \frac{\partial}{\partial y} + \omega^2 \mu \right) H_z = 0 \quad (1.4)$$

$$\left(\frac{\partial}{\partial x} \frac{1}{\rho_x} \frac{\partial}{\partial x} + \frac{\partial}{\partial y} \frac{1}{\rho_y} \frac{\partial}{\partial y} + \frac{\omega^2}{B} \right) p = 0 \quad (1.5)$$

Equation 1.4 describes transverse electric (TE) EM waves propagating in the z-direction, in which ω is frequency in radians and H the magnetic field. Equation 1.5 describes fluid acoustic waves propagating in a medium with anisotropic density in the x-y plane. Subscripts in Equations 1.4 and 1.5 indicate the directional component. A comparison of the equations reveals ε_x corresponds to ρ_y , ε_y corresponds to ρ_x , and μ corresponds to $1/B$. An analogous equation pair can be made between the governing differential equation for transverse magnetic (TM) waves and Equation 1.5, with ε and μ switched and the electric field replacing the magnetic field. This equivalence in principle allows analytical and mathematical findings in TE and TM EM systems to be applied to fluid acoustic systems. It is important though that only one of the EM properties be anisotropic, since bulk modulus cannot be anisotropic. Analogies with anisotropy in both ε and μ can only be done with general elastic waves.

Given this mathematical equivalence between acoustic and certain EM systems, the next point of comparison is naturally available material properties. Unlike the positive, real, single values typical in fluid acoustics, in electromagnetism it is accepted that the permittivity and permeability of a material can vary strongly with frequency in ranges of interest, even taking negative values over limited bands. Physically, this is expected in EM since the material response is due to electrons and cores interacting locally and in bulk. Using a simplistic view of this as an array of mass pairs connected by a spring, such systems naturally have frequency dependent response amplitudes and phases to driving forces, with naturally occurring resonances causing strong responses.

This mass-spring system analogy is exactly the system proposed by Milton and Willis to achieve unnatural effective densities in elastic and acoustic materials. Nothing physically prohibits density from being dispersive at commonly used frequencies. Instead, microstructures with mass-spring resonances at common acoustic frequencies simply do not occur naturally. This is not the case with bulk modulus, as bubbles can demonstrate. Naturally occurring bubbles in the ocean⁶ and engineered coated spheres⁷ have highly frequency dependent responses, with very large volume changes caused by harmonic applied pressures at frequencies of interest.

Effective Medium Theory

Determining effective properties of acoustic metamaterials requires understanding the principles and assumptions of effective medium theory. According to Watt et al.⁸, effective medium theory in acoustics and elastic media theory arose from the need to deal with microscopically heterogeneous media in a practical manner, the same reason as in electromagnetism and other fields. For macroscopic scale engineering, it is not practical or necessary to solve the exact elastic equations for a material's microstructure to describe how it behaves. This would require complete knowledge of the microstructure and an unattainable amount of computing power. Instead, simplified first order approximations like Equations 1.1 and 1.2 are used with analytically or empirically determined properties, which is sufficient for practical purposes. Assignment of empirical properties to the microscopically heterogeneous material replaces the complex local interactions and specific sample details with an average response.

While this homogenization concept is general, the specific analytical effective medium theory derived by Watt et al. is limited to the static and quasi-static effective properties of elastic media, with effective properties modeled as small perturbations to the volume average properties. As a result, bounds from energy considerations limit values to the positive range, which is expected intuitively in the static limit. Effective medium theory for dynamics elastic properties is considerably different and has been investigated theoretically in depth starting with a series of papers by Berryman⁹ beginning in 1979. Extending work done by Mal and Knopoff¹⁰, Berryman proposed a general method of obtaining the effective properties of a composite formed by inclusions in a matrix, called the multiple-scattering technique today. He then applied this method to specific designs¹¹⁻¹², demonstrating elastic properties different from the volume average. The technique is a simplification of the Green's function method of solving the many-body scattering problem for waves, valid under the assumption of a wavelength much larger than the microstructure periodicity.

Two groups have further developed the theory specifically for effective densities. Sheng et al. analyzed the homogenization of cubic packed polymer coated lead spheres in an epoxy matrix, deriving the effective density of this microstructure when the bulk modulus is defined as the volume average¹³. The predicted transmission band gaps associated with negative density matched experimentally found transmission band gaps in a sample tested earlier¹⁴. Milton and Willis generalized the effective density analysis to arbitrary elastic and acoustic media with hidden mass density elements, modeling inclusions as generic mass-spring-dampers. Near the resonance frequency of these inclusions, the effective density was shown to be altered considerably from the volume average value, with the same mathematical form as a damped simple harmonic oscillator.

While the preceding analytical methods of determined effective properties are sufficient for simple metamaterial designs, another method is needed for complex designs. Effective properties for these designs can be obtained using the reflection and transmission (RT) method detailed by Fokin et al.¹⁵. This method uses RT coefficients from experiments or simulations of

a micro-structured sample to determine the properties a homogeneous sample should have to achieve the same RT coefficients. Knowledge or assumption of the metamaterial thickness and number of complete effective wavelengths inside the slab are required in this method to overcome the existence of multiple index n and impedance z combinations that cause the same RT coefficients. Details of several methods to resolve this issue can be found in the manuscript.

Finally, despite the preceding and numerous other works covering effective properties and extraction routines, no standard guidelines have been established on how subwavelength a unit cell must be for effective medium theory to apply. Cost and fabrication issues may dictate a metamaterial have the largest possible microstructure dimensions, which runs counter to the effective medium theory assumption of unit cell dimensions much smaller than the wavelength. Since the work presented here focused on sub-diffraction limit imaging and related physics, the guidelines are set as follows. Although $\lambda/2$ is the nominal diffraction limit, the unit cell dimension in the direction of propagation should be smaller than $\lambda/4$ since quarter wave plates are considered devices, not materials. This requires selection of an appropriate reference speed, for which logical options are the matrix material phase speed (for designs with discrete inclusions), volume average speed, or effective phase speed. The effective phase speed should be the preferred option, but the issue becomes muddled since phase speeds are complex and the real component is often zero in resonant metamaterials. Accordingly, the effective phase speed is used in non-resonant metamaterials and the matrix phase speed is used for resonant metamaterials.

Historical Engineered Acoustic Materials

Before presenting the acoustic metamaterials developed in this work, it is important to acknowledge phononic crystals, which preceded metamaterials in the field of engineered acoustic materials. These crystals are composed of periodic high impedance inclusions in a matrix, with the matrix phase speed significantly slower than the inclusion phase speed¹⁵. Many unusual acoustic phenomena similar to those in metamaterials including band gaps, focusing, negative refraction, tunneling, and wave guiding were predicted and demonstrated at frequencies corresponding to wavelengths in the matrix material equal to twice the lattice periodicity or smaller¹⁶⁻²⁷.

Since effective medium cannot apply at these wavelengths, analysis of these materials focuses on the band structure. Band structures are acquired by viewing the system as a perfectly ordered infinite lattice of scattering inclusions and determining under what conditions harmonic waves may exist by satisfying the Bloch condition²⁸. Near Brillouin zone edges and in bands above the lowest acoustic branch, gaps and significant anomalous dispersion exist, which leads to the unusual energy propagation directions behind the unusual phenomena. Physically, this means the effects are caused by the interference of scattered waves from adjacent or nearby inclusions, making them highly sensitive to frequency and angle of incidence. In no way were the cited works' effects related to anomalous quantum phonon effects, since acoustic energy levels are a continuum at the temperature and length scales of interest.

The observation of negative refraction in face-centered-cubic packed tungsten carbide beads in water²² is an example of phononic crystal behavior very similar to the negative acoustic index metamaterial presented in Chapters 4 and 5. At wavelengths in water just below the bead center-to-center spacing, numerical band structure analysis showed anomalous behavior around the [111] direction of lattice near the Brillouin zone edge. Cross-sections of the equi-frequency surfaces at these frequencies showed local curvature convex to the origin in this direction, which implied diverging energy rays in water normally incident on a flat slab of crystal around the [111] direction should refract in the negative direction and refocus, which was experimentally observed. The key point is the negative refraction was observed, not negative refractive index. Since the crystal unit cells are larger than the wavelength, effective properties cannot be assigned leaving refractive index undefined. This made the focusing diffraction limited and highly sensitive to direction and frequency, as was also observed in the experiments.

Metamaterial Approaches and Dissertation Outline

Three methods were used in this work to decrease unit cell sizes from the length scales found in phononic crystals to the deep subwavelength sizes needed for application of effective medium theory. The two passive methods were asymmetric microstructure geometries and local resonance, while the active method utilized driven electromechanical elements. Similar to phononic crystals, the asymmetric microstructure method took advantage of the wide range of naturally available acoustic properties and used high contrast materials. However, instead of relying on interference from nearby scattering inclusions, the materials were arranged in deep subwavelength lattices with low symmetry to achieve asymmetric response. Locally resonant acoustic metamaterials used the approach of EM metamaterials, with deep subwavelength mechanical resonators arranged in a lattice achieving strong effects near resonance. Finally, active acoustic metamaterials gained their unique properties from electromechanical elements coherently injecting energy into the system.

Chapters 2 and 3 cover the development of an anisotropic density acoustic metamaterial using a deep subwavelength asymmetric microstructure, with an acoustic hyperlens as the target application. First, the physics behind the hyperlens imaging method are presented and necessary material properties identified. A simple air-brass microstructure is then shown to satisfy the necessary property requirements. Experimental demonstration of robust far-field imaging of sub-diffraction limit sound patterns follows, with a detailed numerical analysis of the brass vibrations provided to address treatment of the metamaterial as a fluid despite the use of elastic materials. Future directions in this field focused on application aspects including increased magnification and flat interfaces follow, with preliminary simulation results shown as available.

Chapters 4 and 5 cover the development of a negative acoustic index metamaterial using the local resonance method. After providing a background on negative acoustic property metamaterials, the negative acoustic index metamaterial consisting of Helmholtz and rod-spring resonators tested here is presented. The combination is shown in simulations to attain a

negative real component of acoustic refractive index, with both real components of bulk modulus and density attaining negative values over the frequency band. Subsequent experimental results are then presented showing a negative real component of index was attained, but intrinsic material loss and design issues created a large imaginary index component corresponding to loss that limits the design application prospects. Future research directions on methods to overcome intrinsic loss conclude the chapter, including use of coupled resonators and resonator designs optimized specifically to improve loss tolerance.

Chapter 6 presents numerical work done towards extending the acoustic hyperlens and negative acoustic index metamaterials to 3D and developing an active acoustic metamaterial to overcome the loss and bandwidth issues in passive negative property acoustic metamaterials. 3D generalization of the cylindrical acoustic hyperlens design is shown to be straightforward, with simulations showing successful magnification of sub-diffraction speakers analogous to the 2D case. 3D generalization of the proposed loss tolerant negative acoustic index is also shown to be straightforward, although the loss tolerance is slightly reduced compared to the 2D case. Finally, after a presentation on active acoustic metamaterial physics and previous work, investigations into the possibility of attaining practical acoustic gain levels and tunable bulk modulus conclude the chapter. Gain is found to be possible with good design within limited frequency windows, but the work on tunable bulk modulus is inconclusive, particularly with regards to negative values.

Chapter 7 summarizes the preceding work and outlines the outstanding problems and possible solutions that may be investigated in future acoustic metamaterials research.

Chapter 2 – Anisotropic Acoustic Metamaterials for Hyperlens

Introduction

Although the creation of negative index materials described in the Chapters 4 and 5 drew a majority of the initial interest, metamaterials do not need negative properties to be of great scientific and practical interest. This is particularly true in acoustics, where neither negative properties nor resonance are needed to achieve novel new properties. In this chapter, the new property of interest is anisotropy in fluids. Unlike elastic materials in which anisotropy is unsurprising, fluids are almost always treated as isotropic. An anisotropic fluid would be a unique addition to fluid acoustics, opening the door to both the acoustic hyperlens pursued in this work²⁹ and the acoustic analogs of transformation optics developments, such as energy trapping³⁰ and cloaking³¹⁻³³.

Hyperlens are a straightforward application of anisotropic material properties originally proposed in EM to achieve far-field imaging of sub-diffraction limit objects. Information contained in evanescent waves is captured prior to decay in a lens that both permits its propagation and magnifies it sufficiently to be propagating at the exit³⁴⁻³⁵. In the original proposal, anisotropic permittivity with one positive and one negative component fulfilled the required support of high wavevector components as propagating waves instead of evanescent waves. Arranging this material in a cylindrical shell completed the device, with magnification during propagation in the outwards radial direction converting evanescent information at the hyperlens input into propagating waves in the media at the lens exit. The first experimental hyperlens demonstration utilized alternating concentric deep subwavelength cylindrical shells of metal and dielectric to achieve the anisotropy and successfully image the word “ON”, with $\lambda/4$ line-spacing in the hyperlens far-field³⁶.

As the diffraction limit is intrinsic to all wave phenomena governed by the standard wave equation, conventional acoustic imaging is also limited by the sound wavelength. In this chapter, the principles of far-field subwavelength imaging using a hyperlens to overcome this limit are presented and the necessary material properties identified. A 2D acoustic metamaterial consisting of alternating layers of air and brass is then shown analytically to attain the necessary anisotropy, with confirmation from effective properties determined from simulated microstructures.

Hyperlens Theory

The term hyperlens was chosen due to the hyperbolic dispersion utilized in the EM far-field imaging lens proposal by Jacob et al.³⁵. Hyperbolic dispersion in a 2D system was shown in principle to permit infinite resolution in the one direction, called the transverse direction here. This can be understood through the equations governing dispersion in 2D systems. The acoustic versions of these are provided in Equation 2.1 for the Cartesian coordinate system and Equation 2.2 for the cylindrical coordinate system.

$$\frac{k_x^2}{\rho_x} + \frac{k_y^2}{\rho_y} = \frac{\omega^2}{B} \quad (2.1)$$

$$\frac{k_r^2}{\rho_r} + \frac{k_\theta^2}{\rho_\theta} = \frac{\omega^2}{B} \quad (2.2)$$

In Equation 2.1, ω is the frequency, B is the effective bulk modulus, k_x and k_y are the wave-vector components along the x and y directions respectively, and ρ_x and ρ_y are the effective densities along the x and y directions. The terms are the analogous in Equation 2.2 except the directions are the radial direction indicated by subscript r and azimuthal (angular) direction indicated by subscript θ . The general derivation of these equations has been done previously³⁷. The subscript ordering in these equations differ from the EM versions because fluid acoustic waves are longitudinal.

At a given frequency, Equation 2.1 defines three possible equi-frequency contour shapes in wave-vector space shown in Figure 2.1. The contour types for Equation 2.2 are identical with the x and y subscripts changed to r and θ . Normal fluids have isotropic density, resulting in the red circle equi-frequency contour. Anisotropic density with positive density components and $\rho_y > \rho_x$ results in the blue ellipse equi-frequency contour. Finally, anisotropic density with negative ρ_y greater in magnitude than positive ρ_x produces the black hyperbolic contour.

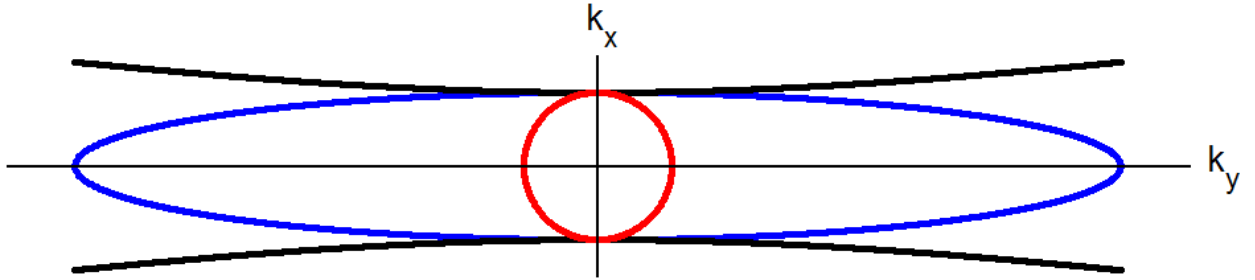


Figure 2.1 Possible equi-frequency contours in a 2D anisotropic acoustic metamaterial. The red line denotes isotropic density, the blue line denotes anisotropic density with positive density components, and the black line denotes anisotropic density with negative ρ_y . In both anisotropic cases, ρ_y is greater in magnitude than ρ_x .

To understand the implications of these dispersion contours, assume two finite dimension flat speakers are projecting sound at a given frequency in the x -direction towards a slab of the material. Spatially Fourier transforming the generated sound pattern in the y -direction reveals it is composed of a broad band of k_y components. Each component is associated with information at a specific length scale, with higher k_y corresponding to smaller length details. The loss of information associated with k_y components removes features of the corresponding lengths from the image. For example, if the spacing between the two speakers corresponds to a range of non-propagating k_y , this information is lost and the measured sound in the far-field will appear to be from a single source.

In the isotropic and double positive density cases, only the portion of k_y components inside the circle or ellipse limits will propagate in the material, with the rest lost to evanescent decay. Anisotropic double positive density with increased ρ_y improves the situation by supporting higher k_y , which increases resolution over the isotropic case. Anisotropic density with opposite signs theoretically improves the situation further by supporting all k_y , which in principle allows infinite transverse resolution. Of course, the resolution is not actually infinite in real systems for two main reasons. On the theoretical side, the effective medium approximation fails at the length scale of the microstructure, capping the largest supported k_y . On the practical side, negative properties in passive materials are always accompanied by loss which damps and distorts waves, limiting the largest k_y that can be considered propagating.

In addition to supporting the largest k_y possible, it is equally important in the hyperlens imaging method that the equi-frequency contours be as flat as possible. Curvature in an equi-frequency contour causes different wavevector components to propagate in different directions defined by the group velocity. The group velocity points in the direction normal to the equi-frequency contour at each k_y , meaning elliptic dispersion causes a sound beam to spread and hyperbolic dispersion causes a sound beam to initially focus. Neither effect is desirable since the image distortion is dependent on the sound source and is not generally reversible. Mathematically, this finding removes the practical importance of hyperbolic vs. elliptic equi-frequency contours, since the curvature at the extremes of both blurs the associated k_y information regardless. What is important is to attain the largest density anisotropy magnitude possible irrespective of signs to create the flattest equi-frequency contours.

Given this criterion, the ideal equi-frequency contour in a 2D system is a pair of horizontal lines created by an infinite positive or negative ρ_y in the coordinate system of Figure 2.1. Materials with this dispersion would support propagation of all k_y and cause all to propagate in the same direction with the same speed. The key to achieving magnification is using these flat dispersion materials in an appropriate coordinate system, which can be understood using the following examples. In the first case shown in Figure 2.2 (Left), two speakers below the diffraction limit in size and separation are placed near one interface of a rectangular layer of material with flat equi-frequency contours in the Cartesian coordinate system. Support of all k_y allows the sound pattern to transfer across the material without loss of resolution. However, no magnification occurred, leaving subwavelength information in their original k_y components, which are still prohibited from propagating in the surrounding medium. These components are still lost in far-field measurements.

Next, consider the same two speakers at the inner interface of a half-cylindrical shell with flat dispersion in cylindrical coordinates shown in Figure 2.2 (Right). Infinite ρ_θ allows information to travel in the r direction without distortion in the θ direction. However, as the wave propagates to larger radii, the same angular distribution corresponds to a larger actual arc-length, meaning magnification occurs. Thus, at the exit, the sound pattern appears to be a larger by a factor equal to the ratio of the outer to inner radius at the cost of an amplitude reduction due to spread of energy over a larger arc. All information in the original sound

pattern has been compressed into lower k_θ at the exit, including a portion of the previously non-propagating sub-diffraction limit information that can now be retrieved in the far-field.

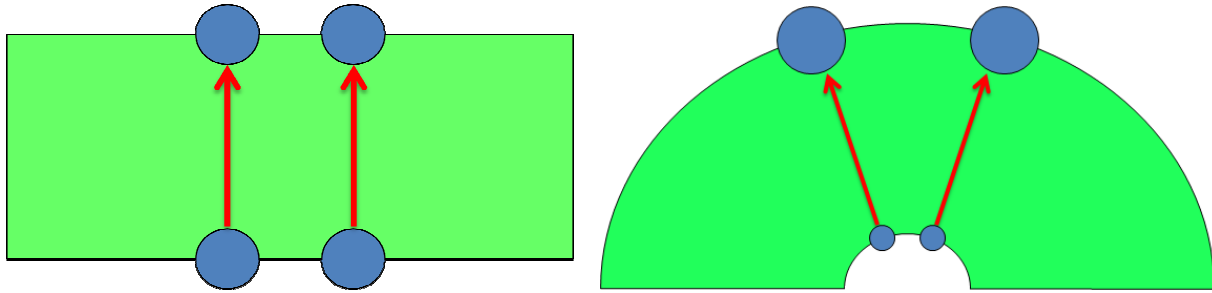


Figure 2.2 Imaging using flat dispersion lenses in (Left) rectangular Cartesian coordinates, and (Right) cylindrical coordinates.

Anisotropic Acoustic Metamaterial Design

In acoustics, natural material property availability provides guidance when choosing between hyperbolic or elliptic contours to achieve the flattest possible equi-frequency contours. Though wide in magnitude, all natural fluid properties are positive, discouraging hyperbolic contours. The necessary negative density for hyperbolic contours can only be generated using resonant metamaterials such as the design proposed by Ao and Chan³⁸. As covered in the negative acoustic index metamaterial chapters, passive resonant metamaterials suffer from significant intrinsic loss and limited bandwidth. Both effects would detract from the hyperlens imaging technique since the magnification factor depends on propagation distance and in principle operates at any frequency. Instead, the wide range of naturally available densities was used here to create a 2D highly anisotropic acoustic metamaterial with extremely wide elliptic equi-frequency contours. Alternating layers of brass and air shown in Figure 2.3 form the microstructure of the metamaterial. Throughout this section, the x -direction refers to the direction parallel with a brass layer and the y -direction refers to the direction perpendicular to a brass layer.

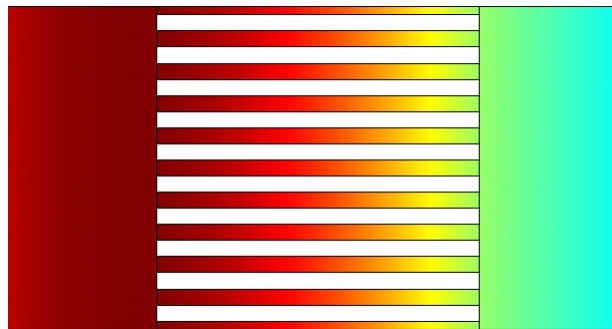


Figure 2.3 Simulation of the metamaterial formed from alternating layers of brass (white) and air (color) to extract x -direction properties. The x -direction is parallel and y -direction perpendicular to a brass layer. The air regions beyond the brass layers are the ends of waveguides used in the simulation.

Local resonance is not utilized in this design, allowing effective properties to be determined from simple analytical relations. Provided the layers and periodicity are sufficiently subwavelength, the effective bulk modulus and densities of this metamaterial can be determined using Equations 2.3-2.5.

$$\frac{1}{\rho_x} = \frac{f}{\rho_1} + \frac{1-f}{\rho_2} \quad (2.3)$$

$$\rho_y = f\rho_1 + (1-f)\rho_2 \quad (2.4)$$

$$\frac{1}{B} = \frac{f}{B_1} + \frac{1-f}{B_2} \quad (2.5)$$

In these equations, f is the volume filling fraction of the fins, ρ_1 and B_1 are the fin material density and bulk modulus respectively, and ρ_2 and B_2 are the filling fluid density and bulk modulus respectively. These equations have the same form as the relations governing series and parallel combination of electrical resistors and can be obtained several ways. The simplest is to take advantage of the analogy between TM polarized electromagnetic waves and acoustic waves described in Chapter 1 and borrow the effective medium properties for electromagnetic waves³⁵ with the necessary parameter substitutions.

Equations 2.3 and 2.4 show the fin material density must be as large as possible relative to the fluid density to create flat equi-frequency contours. This explains the choice of brass and air, since brass has a density about 7000 times that of air. Using the material properties in Table 2.1, the layered air-brass metamaterial has effective densities of 2.4 kg/m³ in the x-direction and 4251 kg/m³ in the y-direction, and an effective bulk modulus of 284 kPa. This large density anisotropy increases the maximum supported transverse wavevector by a factor of 60 vs. air.

Table 2.1 Hyperlens Material Properties

<i>Material</i>	<i>Density (kg/m³)</i>	<i>Sound speed (m/s)</i>	<i>Young's Modulus (GPa)</i>	<i>Adiabatic Bulk Modulus</i>	<i>Poisson Ratio</i>
Air	1.21	343		142 kPa	
Brass	8500	4700	104	75 GPa	0.37
Aluminum	2700		71		0.33
Stainless steel	7700		19.5		0.28

To verify these analytical relations, effective properties determined using the RT method described in Chapter 1 were obtained from 2D simulations of the metamaterial microstructure using the finite element package COMSOL Multiphysics™ 3.4 with the Acoustics and Structural Mechanics Modules. The simulation domain consisted of a layer of the metamaterial situated between two air filled waveguides, with Figure 2.3 showing the metamaterial layer oriented for x-direction property determination and the ends of the connecting waveguides. Air was modeled as an isotropic fluid and brass as an isotropic elastic solid. Radiation boundary

conditions were applied to the outer waveguide ends, with one end assigned to input a 1 Pa plane wave towards the metamaterial. These boundary conditions allow user defined plane waves to enter and allow all incident plane waves to leave. The air-brass boundaries were assigned continuity of normal acceleration conditions and zero shear stress, appropriate for an inviscid fluid. Remaining fluid boundaries were assigned hard boundary conditions and elastic boundaries assigned roller conditions. The extracted effective properties in the x and y directions are shown in Figures 2.4 and 2.5. Over the frequency range tested, the values agreed almost exactly with the analytical predictions.

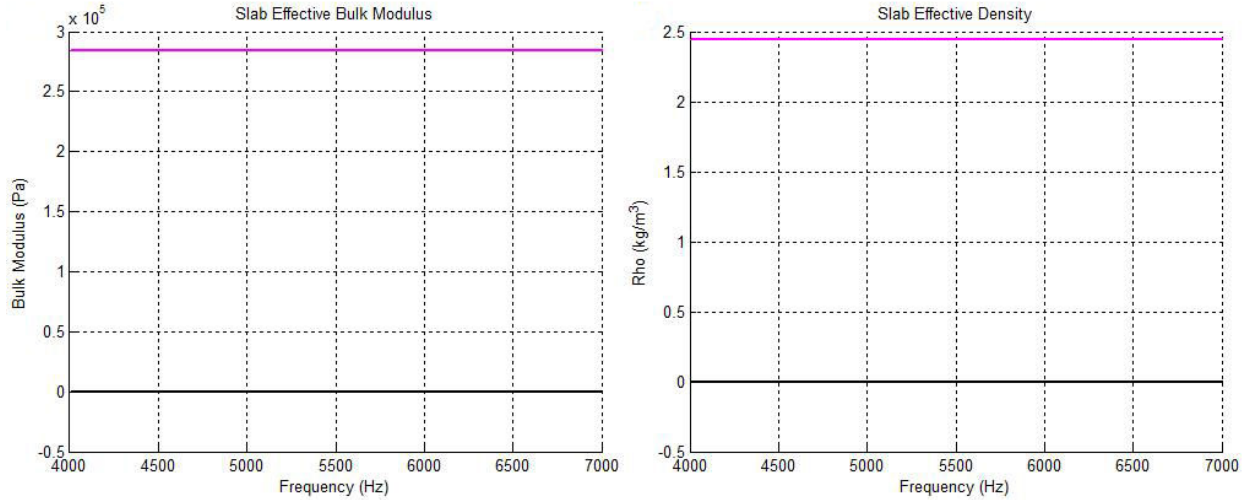


Figure 2.4 Extracted (Left) bulk modulus and (Right) mass density of the air/brass metamaterial in the x -direction. Real components are plotted in magenta and imaginary in black.

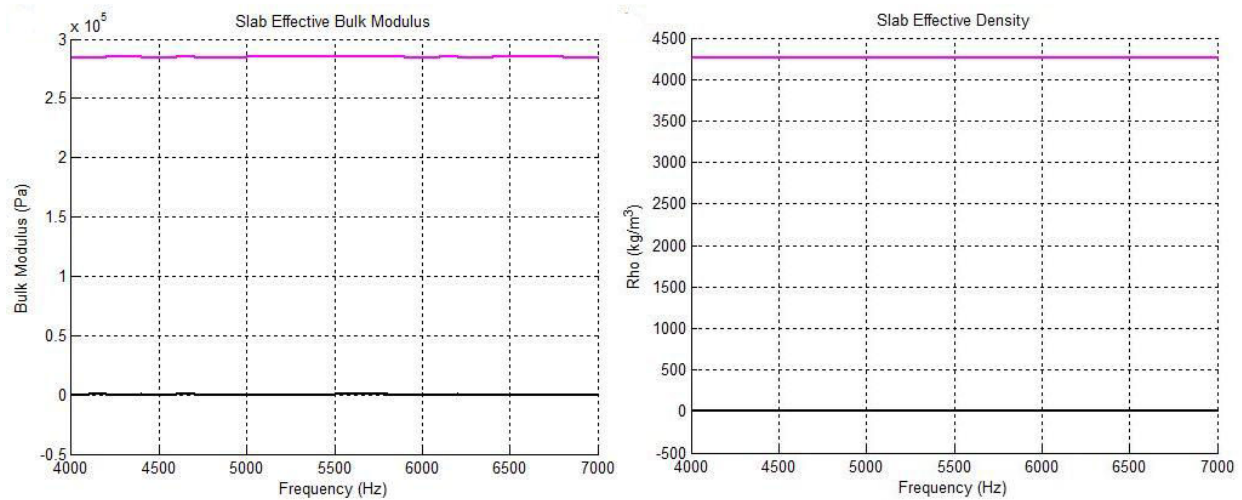


Figure 2.5 Extracted (Left) bulk modulus and (Right) mass density of the air/brass metamaterial in the y -direction. Real components are plotted in magenta and imaginary in black.

Shear Mode Coupling

One valid question concerning the preceding work is the neglect of the ability of brass to support shear motion. Previous work has shown theoretically that a large density contrast in deep subwavelength solid-fluid microstructures makes the influence of these motions negligible³⁹. To further examine this issue, a study was done on the transfer of energy from air to shear modes in brass at an interface of air and brass half-spaces. The amount of energy coupled from a plane wave in air into the in-plane shear mode of brass at the interface as a function of input angle is given in Equation 2.6, with the terms defined in Equation 2.7-2.12. These equations have been derived previously, for example by Brekhovskikh⁴⁰.

$$\frac{E_{shear}}{E_{in}} = \frac{\rho_{brass} \tan(\theta_{in})}{\rho_{air} \tan(\theta_{shear})} |T_{shear}|^2 \quad (2.6)$$

$$T_{shear} = \frac{P_{shear}}{P_{in}} = - \frac{2\rho_{air} Z_{long} \sin(2\theta_{shear})}{\rho_{brass} (Z_{long} \cos^2(2\theta_{shear}) + Z_{shear} \sin^2(2\theta_{shear}) + Z)} \quad (2.7)$$

$$Z = \frac{\rho_{air} c_{air}}{\cos(\theta_{in})} \quad (2.8)$$

$$Z_{long} = \frac{\rho_{brass} c_{long}}{\cos(\theta_{long})} \quad (2.9)$$

$$Z_{shear} = \frac{\rho_{brass} c_{shear}}{\cos(\theta_{shear})} \quad (2.10)$$

$$\theta_{long} = \arcsin\left(\frac{c_{long} \times \sin(\theta_{in})}{c_{air}}\right) \quad (2.11)$$

$$\theta_{shear} = \arcsin\left(\frac{c_{shear} \times \sin(\theta_{in})}{c_{air}}\right) \quad (2.12)$$

In these equations, P is pressure, E is energy flux, c is phase speed, and θ the angle between the wavevector and interface normal. The subscript "long" refers to the longitudinal mode in the elastic material, "shear" refers to the in-plane transverse polarized mode in the solid, and "in" refers to the input wave. Using the values in Table 2.1, the ratio of energy coupled to the brass shear mode from the air wave was calculated and is plotted in Figure 2.6. As expected, the coupling from air to the shear mode in brass is extremely small even at the optimum coupling angle, supporting the assertion that shear motion may be neglected.

Of course, this simple analysis does not guarantee shear waves will not be excited in this metamaterial. Finite brass layers will also support waves confined to a layer with mixed polarization such as Lamb waves which may be excitable. Determining whether these modes are relevant requires analyzing the stress in the brass layers. Shear waves in a brass layer should travel much faster than the homogenized material speed in this direction. If such waves are excited enough to be significant in the brass, long spatial oscillations in the brass stress pattern should dominate the short length oscillations associated with the homogenized speed. Of course, the energy carried by the brass must also be greater than the air to be significant.

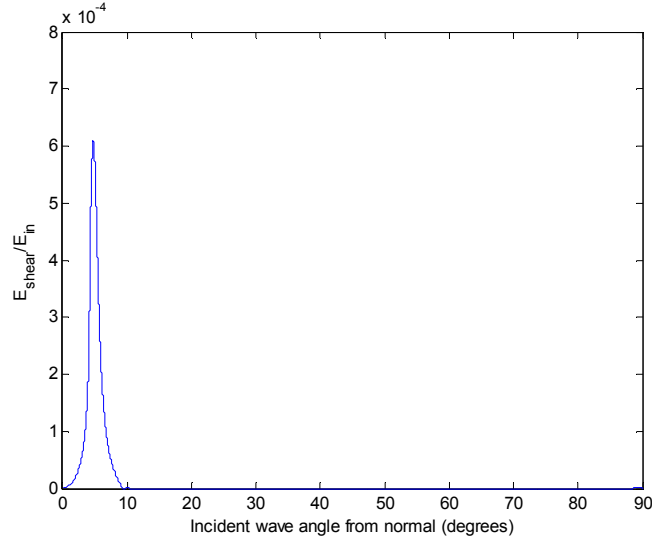


Figure 2.6 Fraction of energy coupled to the brass pure shear mode from the input plane wave in air at the interface between half-spaces.

Summary

This chapter discussed the theory and history behind far-field sub-diffraction limit imaging using the hyperlens method. Analysis of the dispersion relation revealed strong density anisotropy irrespective of component signs is the key to this method in acoustics. Alternating layers of air and brass were shown to attain the necessary anisotropy through theoretical and numerical analysis. The issue of shear modes in brass layers was then examined at the interface of a half-space, and further details on design specific analysis procedures detailed. This work fulfills the prerequisites to creation of an acoustic hyperlens, which allowed construction and testing of the device detailed in the next chapter.

Chapter 3 – Acoustic Hyperlens Experiments

Introduction

In the preceding chapter, it was shown that far-field sub-diffraction imaging in acoustics is possible using a metamaterial with highly anisotropic density, and that alternating layers of air and brass fulfilled this requirement with a 3 order of magnitude density contrast. In this chapter, the design and experimental results of a 2D acoustic hyperlens utilizing this air-brass metamaterial in a cylindrical geometry with 8 times magnifying power are presented. A pair and trio of sub-diffraction limit speakers with sub-diffraction limit spacing are shown to be successfully magnified into distinct propagating beams in the far-field, with further examination of the far-field pressure pattern along a beam confirming the conversion of evanescent components to propagating components. Brass and air acceleration profiles from simulations of the hyperlens are also presented to verify transverse modes are not important in this metamaterial when homogenizing the microstructure. Methods of attaining further magnification and flat input/output interfaces for application purposes are presented as future directions in hyperlens development to conclude this chapter.

Acoustic Hyperlens Design and Experimental Setup

Conversion of the air-brass anisotropic metamaterial presented in Chapter 2 from Cartesian to cylindrical coordinates was straightforward, with the hyperlens implementation shown in Figure 3.1. The acoustic hyperlens consisted of 36 brass fins 3 mm tall extending from an inner radius of 3.1 cm to an outer radius of 21.8 cm, corresponding to 8 times magnification. Each brass fin occupied 2.5 degrees in the angular direction, with 2.5 degrees occupied by air between fins. The resultant fins expand from approximately 1 mm wide at the inner radius to 8 mm wide at the outer radius. The hyperlens was machined on one side of a 0.5 inch thick brass plate using a two-axis computer controlled vertical mill, leaving the fins on a 9.7 mm thick substrate. 0.25 inch thick aluminum plates formed the top cover sheet, confining sound propagation to two dimensions in the air-brass metamaterial.



Figure 3.1 Acoustic hyperlens used in experiments with the cover sheet removed.

Sound patterns were generated using 10mm diameter Model Rectifier Corporation speakers suitably arranged around the inner hyperlens radius on custom fabricated mounts. Pressure signals were measured using a Horn™ 10 mm diameter electret condenser microphone connected to a Stanford Research Systems SRS-830 lock-in amplifier. This amplifier supplied a harmonic continuous wave driving voltage to the speakers, which also served as the reference signal in microphone phase measurements. LabVIEW® software was used to scan the driving frequency from 4.2 kHz to 7 kHz at each measurement location and retrieve the microphone response. This frequency range was selected due to the combined limitations of speaker and microphone capabilities, not the hyperlens.

To minimize the effects of the environment, hyperlens experiments were done in a chamber lined with acoustic absorbing foam. Each set of experiments required first positioning the speakers in the desired arrangement near the inner hyperlens radius, with extra care taken with respect to the distances between speakers and hyperlens edge. Once the source positions were verified, the cover plate was installed with weights on top to ensure contact with the brass fins. The microphone was then positioned in a hole in the cover plate corresponding to a specific radius and measurements over the range of driving frequencies were taken at a set of angular positions by rotating the top plate about the hyperlens center axis. Holes not in use during a measurement were plugged to prevent aberrations. By repeating the angular scanning with the microphone in each of the holes, the pressure field in the region 0.4 cm to 9.9 cm in the radial direction beyond the outer lens edge spanning the full 180 degrees in the angular direction could be mapped. Control experiments followed the same procedure except the hyperlens plate was flipped over to the un-machined side. Very small spacers were used to maintain the 3 mm gap between the plate and cover sheet. Changing the location of these spacers had no noticeable effect on the output sound pattern.

Experimental Results

In the first set of experiments, two speakers driven in-phase separated by 1.2 cm center-to-center were placed at the inner edge of the hyperlens and imaged in the far-field with and without the hyperlens. The 1.2 cm separation corresponds to $\lambda/6.8$ at 4.2 kHz and $\lambda/4.1$ at 7 kHz, both well below the diffraction limit. The maximum measurement distance of 9.9 cm away from the outer hyperlens edge corresponds to 1.2λ at 4.2 kHz and 2λ at 7.0 kHz, both of which were sufficiently large to determine via phase measurements that the beams leaving the hyperlens were composed primarily of propagating components. The experimental results at 6.6 kHz are shown in Figure 3.2 (Left) along with the results from an effective medium simulation in Figure 3.2 (Right) for comparison. This simulation used the analytically determined effective properties from Chapter 2 in the outlined hyperlens domain.

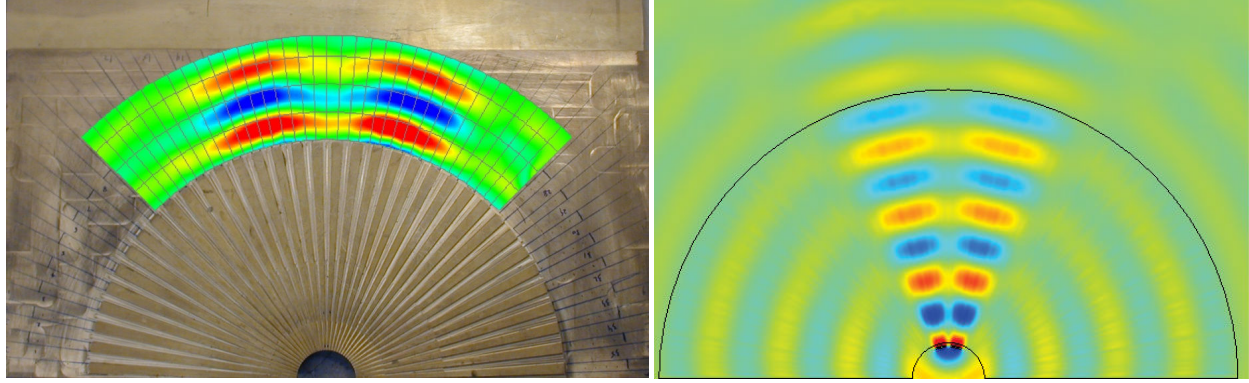


Figure 3.2 Two source hyperlens results. (Left) Experimental acoustic hyperlens with pressure field measurements superimposed. (Right) Simulated acoustic hyperlens pressure field using the analytically determined effective properties.

As predicted from theory and simulation, 8 times magnification by the hyperlens at 6.6 kHz increased the speaker diameters to 1.5λ and separation to 1.85λ at the hyperlens exit. The separation was sufficiently large to generate two distinct beams at the hyperlens exit, and the magnified diameters were large enough for the beams to remain coherent for a significant distance. At the lower tested frequencies the magnified speaker sizes were not as large relative to the wavelength, causing interference effects to appear in the far-field within the measured range. Without the hyperlens, the speakers were indistinguishable in the far-field as shown in the comparison of pressure amplitudes measured along an arc just beyond the hyperlens outer radius in Figure 3.3 (Left). Two distinct peaks are clearly distinguishable in the red curve with the hyperlens, while the control experiment without the hyperlens resulted in the single peak blue curve due to the diffraction limit eliminating the relevant wavevector components in the far-field.

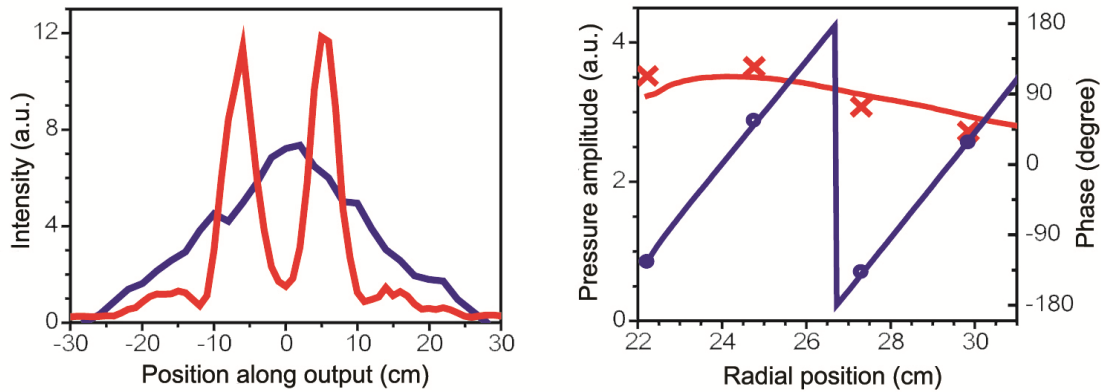


Figure 3.3 Verification of hyperlens effects at 6.6 kHz. (Left) Comparison of pressure amplitude along an arc just beyond hyperlens outer radius with the hyperlens in red and without the hyperlens in blue. (Right) Phase and amplitude measurements, in red and blue respectively, along a beam exiting the hyperlens. The marks are experimental data and the lines are values predicted from simulation.

To quantitatively verify hyperlens functionality, the compression of energy in components that would be evanescent without the hyperlens into propagating components at the exit was examined via the phase and amplitude along the propagation path of one of the beams at 6.6 kHz plotted in Figure 3.3 (Right). Magnification of a source to 1.5λ should result in a beam composed primarily of propagating components, which in cylindrical coordinates should have linear phase dependence with distance and amplitudes that decay approximately as $r^{-1/2}$ due to geometric expansion. The relative amounts of evanescent components can be determined by the radial extent of complex phase and amplitude behavior in a mixture of these components. For this hyperlens at this frequency, the linear phase behavior signals the beam is composed primarily of propagating waves, which the amplitude behavior confirms given the short extent of complex behavior.

One final aspect of this hyperlens of note is the ability to magnify over a broad frequency band. As shown in Figure 3.4, two peaks are observable in the amplitude distribution along the arc just beyond the hyperlens exit over the entire 4.2 kHz to 7.0 kHz frequency range. These peaks maintain the same separation and approximately the same full-width-half-maximum over the entire frequency band, verifying the density anisotropy was large enough to make magnification independent of frequency. This broadband operation was allowed by the use of elliptic equi-frequency contours instead of hyperbolic contours. Elliptic contours do not need negative properties caused by local resonance, eliminating this source of frequency band limitation. However, these contours do not eliminate the Fabry-Perot resonances created by the moderate impedance mismatch between the metamaterial and air. The finite peaks and valleys in transmission created by this impedance mismatch have been decreased in Figure 3.4 by amplitude normalization.

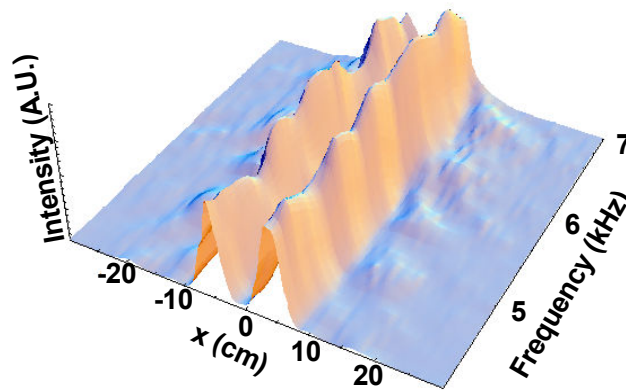


Figure 3.4 Broadband hyperlens performance. The amplitude at each frequency has been normalized to allow plotting on the same figure.

Although the two source experiments agree well with expectations from theory and simulation, one may question how well the hyperlens functions with less symmetric and optimally positioned speaker arrangements. This was investigated in a second set of experiments using

the asymmetric three speaker arrangement shown in Figure 3.5c. Viewed from above, the two speakers spaced 1.2 cm center-to-center used in the first set of experiments were rotated counter-clockwise about the hyperlens origin and a third source was added 2 cm center-to-center clockwise from the right speaker of the pair. The speaker distances from the hyperlens edge were also varied, with the centermost speaker 1 mm away from the hyperlens inner edge, the adjacent 2 mm away, and the new third speaker 3 mm away.

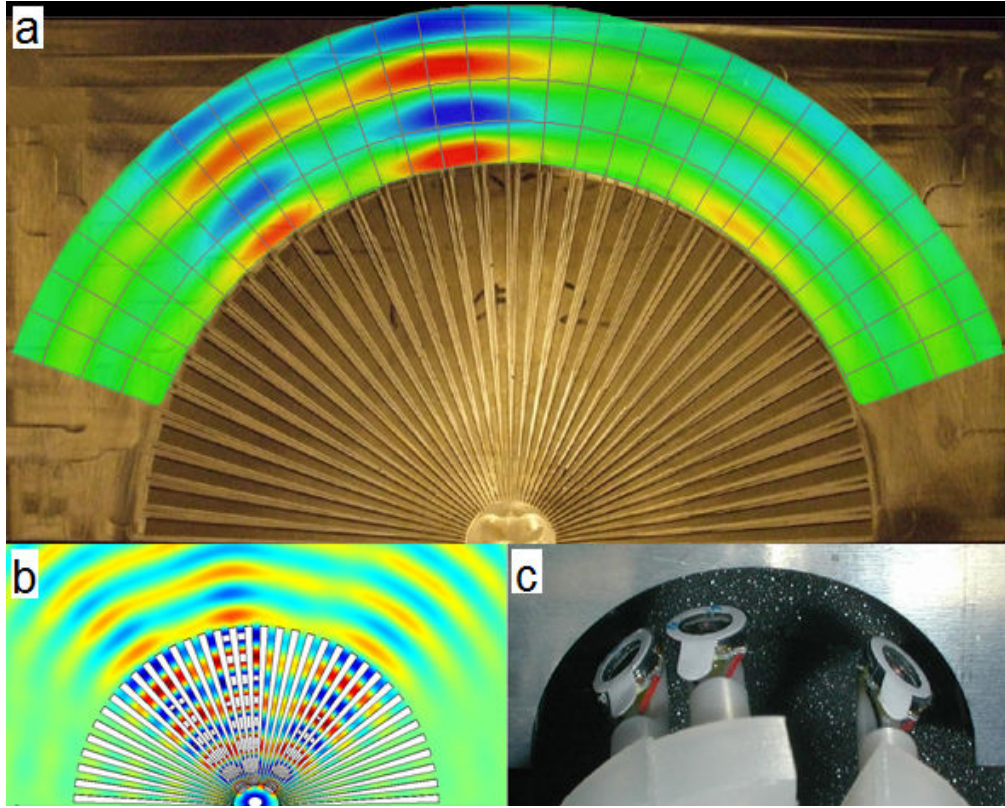


Figure 3.5 Hyperlens imaging of three speaker source. (a) Experimental results superimposed on hyperlens, (b) 2D simulation of three speaker setup with high pressure amplitudes inside hyperlens saturated to white, (c) Trio of speakers used in experiment.

The results of these experiments at 6.6 kHz are shown in Figure 3.5a. Three beams of can be clearly seen at 6.6 kHz in the far-field of the hyperlens, with the effect of different speaker-hyperlens distance also clearly observable in the varying amplitudes. The output amplitude was expected to be inversely proportional to the speaker distance from the lens edge, since the amount of evanescent component decay prior to coupling to the lens grows exponentially with distance. These angular distributions and amplitude variations also matched that predicted from 2D simulations modeling the brass fins as elastic, shown in Figure 3.5b.

Internal Hyperlens Fields

Experimental measurements of the pressure field inside the hyperlens to verify the internal beam propagation matched those of a strongly anisotropic metamaterial were found to be

overly disruptive to hyperlens operation. Instead, 3D simulations were done also using COMSOL Multiphysics™ 3.4 to investigate the agreement between effective medium theory and microstructured systems. The 3D simulations consisted of the elastic brass fins, elastic brass substrate, elastic top plate, fluid air, and speakers using the material parameters in Table 2.1. Radiation boundary conditions were applied to outer boundaries of fluid domains to mimic free space, while free boundary conditions were applied to exterior boundaries of elastic domains except at the base, which was fixed. Continuity of normal force/acceleration and zero transverse stresses boundary conditions were applied to the elastic-fluid boundaries. The speaker surfaces were assigned pressure amplitudes of 1 Pa. Tetrahedral mesh elements with a maximum length of $\lambda/5$ were used to discretize the simulation domain, with a finer mesh used in hyperlens. Good agreement was found between the results of this 3D simulation with microstructure shown in Figure 3.6 at 6.6 kHz and the experiments and 2D effective medium simulations in Figure 3.2. This confirms the finite hyperlens thickness did not fundamentally change the physics behind hyperlens operation.

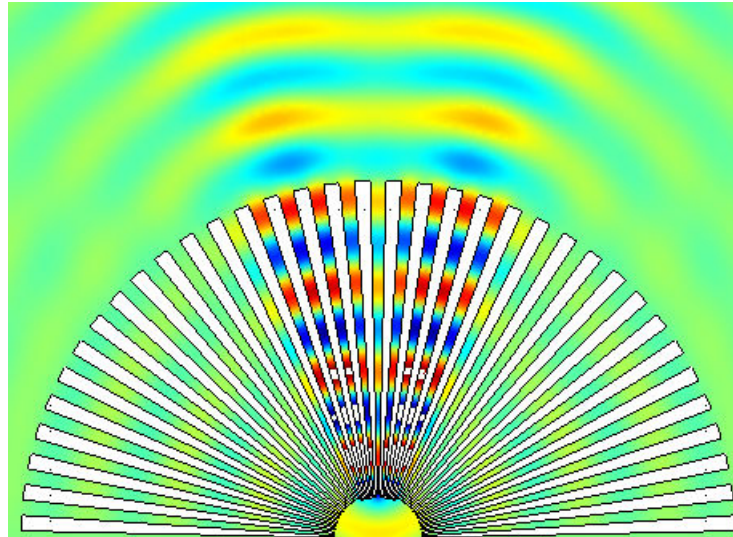


Figure 3.6 Pressure field at hyperlens midplane from 3D simulation of experimental hyperlens. Brass fins are white while pressure field is plotted in color representing local pressure value, with strong pressure values in the inner hyperlens washed out to white as well.

Further verification of the effective medium approximation results can be seen by comparing the accelerations of the brass fins and air in the radial and angular directions shown in Figure 3.7. Examining the acceleration amplitudes first, the angular brass acceleration in Figure 3.7 (Right) is an order of magnitude greater than the radial acceleration in Figure 3.7 (Left), and ratio of the brass to air acceleration is more than an order of magnitude larger in angular direction. These indicate the brass should affect the angular effective density much more, which was born out in the calculated effective properties.

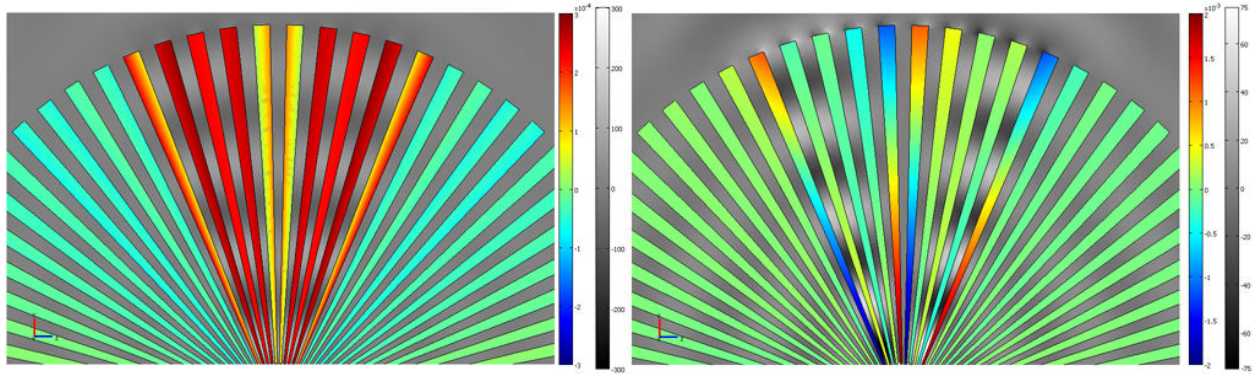


Figure 3.7 Brass and air acceleration components in the (Left) radial direction and (Right) angular direction. The brass acceleration is plotted in rainbow color scale and the air vibrations in gray scale. The color bar and gray scale bar limits (units: m/s^2) in the radial case are $\pm 3 \times 10^{-4}$ and ± 300 respectively, and the analogous limits in the angular case are $\pm 2 \times 10^{-3}$ and ± 75 .

In terms of characterizing the validity of neglecting brass shear motion in the determination of effective properties, two observations can be made from Figure 3.7. In Chapter 2 it was noted that shear waves appear in the brass fin stress fields as oscillations longer in wavelength than in air, with the relative strengths indicative of the importance. Figure 3.7 (Right) shows the brass acceleration periodicity in fact does not match that of air, particularly in the fins at the edges of the sound patterns. However, less than a wavelength appear in each fin making it difficult to determine whether the shear motion is a mode. The second observation is the brass acceleration is multiple orders of magnitude smaller than the air acceleration in both directions. The 6 order of magnitude difference in the radial direction in particular shows the energy was transferred across the hyperlens primarily through the air, making the brass support of shear motion unimportant.

Future Directions

With the successful demonstration of a 2D air filled acoustic hyperlens, the remaining major technical challenges in hyperlens development center on imaging requirements. The three most pressing improvements needed are increasing the resolving power, switching to practical interface shapes, and generalization to 3D. Numerical investigations into possible designs that provide increased magnification and flat interfaces are presented in this section, with 3D generalization covered in Chapter 6.

Increasing the resolution of a hyperlens appears straightforward since the magnification is only a function of geometry. For the cylindrical hyperlens design, logically one need only increase the outer radius or decrease the inner radius to increase magnifying power. However, attention is required to remain in the effective medium limit, described in the following, and addressing phase distortions, which is relevant for the flat interface hyperlens described later. Remaining in the effective medium limit requires a sufficiently subwavelength periodicity throughout the entire lens. Failure to do so results in the situation shown in Figure 3.8 (Right) for the two speaker case, with the effective medium case plotted in Figure 3.8 (Left) for

comparison. The periodicity of the outer hyperlens half of Figure 3.8 (Right) is larger than half a wavelength, prohibiting the effective medium approximation. Loss of k_θ control occurs, with energy transferred to other modes in the air channels resulting in an output sound pattern different from the input pattern.

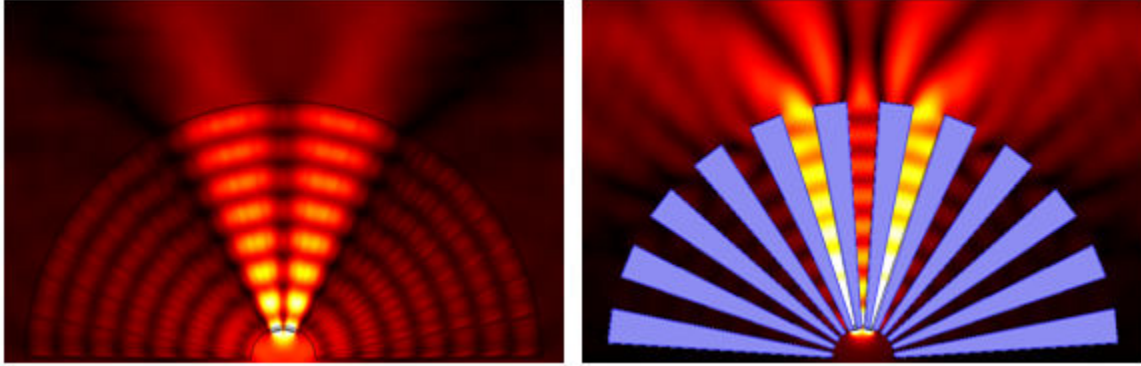


Figure 3.8 Effect of fin periodicities larger than allowed by the effective medium approximation. (Left) Effective medium simulation, (Right) simulation with fin periodicity larger than a wavelength at the exit.

Ideally, the fin thickness and periodicity should be infinitesimally small to allow arbitrarily small inner radii and large outer radii, permitting any designer selected magnification ratio. However, practical fabrication constraints place limits on overall feature sizes, with individual tools limited in range of achievable feature size and machining area. One design that overcomes this challenge cascades multiple layers of hyperlens as shown in Figure 3.9. Each additional layer of hyperlens maintains subwavelength periodicity by increasing the number of fins while retaining the same filling fraction and materials. This maintains the same effective properties throughout the hyperlens, minimizing impedance mismatch effects at the interfaces.

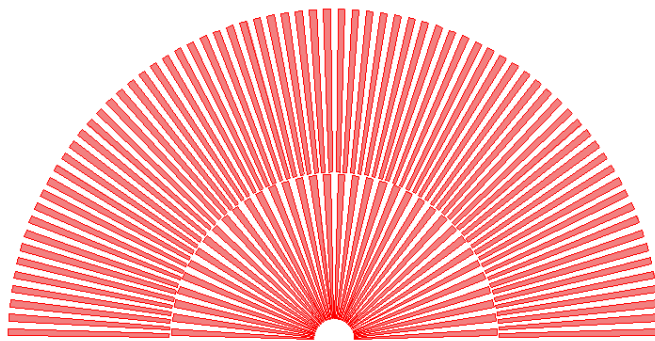


Figure 3.9 Cascaded hyperlens design allowing increased magnification via increased outer radius.

Another issue in acoustic hyperlens development is the choice of shape for the input and output interfaces. As demonstrated in the three speaker source experiments, the hyperlens input edge must be very close to the sound sources to capture evanescent sound components

prior to decay. This may not be possible using a cylindrical inner interface in a practical application such as medical ultrasound, particularly at the length scales associated with MHz frequencies common in this field. For this and other imaging applications, it is preferable to have flat or nearly flat input and output interfaces. Transformation mathematics provides methods to convert the 2D cylindrical design into a flat interface design, as shown in Figure 3.10. The curved lower half of this hyperlens was created using the same transformation as Han⁴¹, except the perpendicular contours were selected.

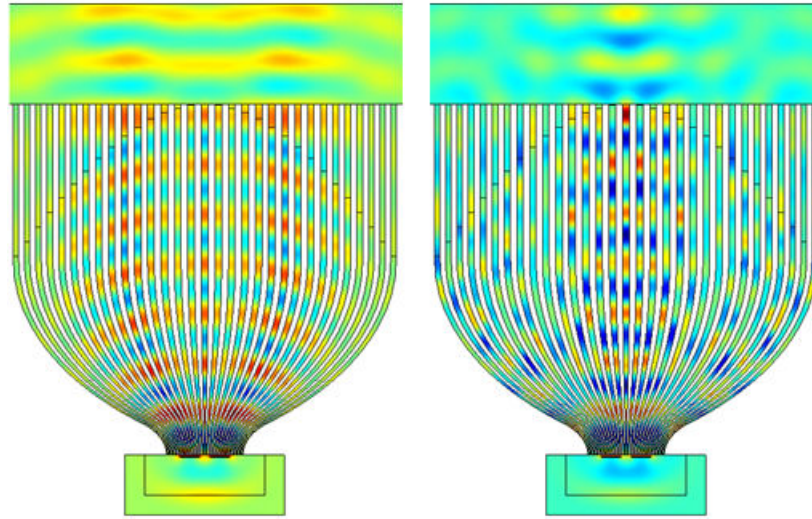


Figure 3.10 Water filled flat hyperlens with phase correction addition using (Left) rigid walls and (Right) elastic brass walls.

Unlike in the extension to 3D, here the longitudinal nature of acoustic waves created an additional problem. Phase speed is independent of local periodicity for longitudinal waves, leading to distortion in the phase front which is not present in the EM version of this design. This distortion is obvious along the horizontal line between the curved and straight sections in Figure 3.10 (Left). To resolve this problem, an additional phase correction lens was added in series on top of the curved hyperlens. This straight section used two fluids with the same impedance but different phase speeds to fill the channels between the fins, allowing phase manipulation through variation of the occupancy ratio. Fins with high density relative to both fluids were still necessary to prevent transverse spread of energy before the phase correction was complete.

The required impedance correction lens length is proportional to the phase speed contrast. Since no fluid with similar impedance to air has a significantly different phase velocity, this means continued use of air as the primary filling fluid would require an impractically long phase correction section. Suitable materials with sufficient speed contrast and similar impedances are available for water, so this was used in both lenses to minimize reflection at the interface. It is important to note though that these materials are moderately hard polymers, so the effects of shear modes and intrinsic loss will need to be examined.

If fins with high density contrast with water were available, this hyperlens would be able to magnify sub-diffraction limit speakers above the diffraction limit at the exit, as shown in Figure 3.10 (left). In this simulation, the fin density was arbitrarily assigned a value 10 times that of brass, while the elastic constants were the standard brass values used in Chapter 2. Using standard brass density and elastic constants for the fins resulted in Figure 3.10 (right). The density ratio between brass and water is approximately 8, which was insufficient to create the flat, wide equi-frequency contours necessary to support high transverse wavevectors. Few evanescent components become propagating in this hyperlens, and the components that do propagate rapidly spread in the transverse direction. As a result, the output sound pattern is characteristic of a single source. No known materials provide a sufficiently large density relative to water, meaning solving this problem will require use of more advanced dispersive microstructures, such as hollow fins or membrane walls, to manipulate local phase velocities at the cost of frequency dependence⁴²⁻⁴³.

Summary

In this chapter, experiments on a non-resonant 2D acoustic hyperlens capable of supporting and magnifying acoustic information including sub-diffraction limit components 8 times as it traversed the lens were presented. A symmetric speaker pair and asymmetric trio of speakers were magnified from their original sub-diffraction limit sizes and spacing into propagating beams in the far-field over a broad band of frequencies, with a detailed examination of the phase and amplitude along one of these beams confirming the magnified pattern consisted primarily of propagating components. The strong sensitivity to source distance from the hyperlens was demonstrated in the three speaker experiments, which matched the expectation of exponential evanescent component decay in the distance between speaker and lens input surface. Finally, microstructured 3D simulations of the hyperlens revealed behavior matching effective medium simulations and in agreement with the neglect of brass shear wave support. With this successful proof of concept demonstration, acoustic hyperlens research can shift to application specific improvements. Increased magnifying power and interface shape improvement were presented here, with 3D generalization presented in Chapter 6.

Chapter 4 – Negative Acoustic Index Metamaterials

Introduction

Achieving negative material properties, particularly negative refractive index n , has been one of the main driving forces behind metamaterial research. The idea of negative n is quite old in EM, with several, including Veselago⁴⁴ more than 40 years ago, theoretically demonstrating negative n would occur if a material with negative ϵ and μ were created. Of great interest on the scientific front are the numerous anomalous physical behaviors predicted to occur in such a material, including negative refraction of propagating waves, reverse Doppler Effect, slow group velocities, and reverse Cherenkov radiation. For acoustic and elastic media, in addition to the analogues of these phenomena, negative material properties would also allow entirely new modes with interesting characteristics previously prohibited by the assumption of positive properties⁴⁵. A successful demonstration of negative refractive index and these phenomena in acoustics would both validate acoustic metamaterial theory and differentiate them from phononic crystals since these phenomena only occur when effective medium theory is valid.

The second motivation for negative material properties are the applications of these unusual physical phenomena, particularly in imaging with the proposal of a perfect lens by Pendry⁴⁶. Pendry theoretically demonstrated that evanescent EM waves incident from a point source in air are enhanced in amplitude when crossing a flat lens with a refractive index of -1 in the idealized zero-loss case. These waves recombine with the negatively refracted propagating waves at a focal point beyond the lens exit, recreating an image of the source unbound by the diffraction limit. While subsequent work⁴⁷ pointed out that model flaws, assumptions, dispersion, and material losses will limit the real world performance of a perfect lens, sub-diffraction limit imaging using enhanced evanescent waves was validated through experimental demonstration⁴⁸. This confirmed sub-diffraction limit imaging is in principle possible in EM and could lead to great advances in optical microscopy and lithography.

Sub-diffraction limit imaging is also possible for acoustic waves using a negative acoustic index metamaterial created by driving the appropriate material properties negative. For loss-less fluids, these properties are bulk modulus and density. A metamaterial with a negative real component of acoustic index caused by the traditionally cited combination of negative real components of bulk modulus and density is called a double negative acoustic metamaterial in this work. Much theoretical and experimental work has been done on acoustic and elastic metamaterials utilizing local resonance to attain negative bulk modulus⁴⁹⁻⁵¹ and negative density^{14,52-55} individually. Experimentally validated bulk modulus resonator designs include Helmholtz (HH) resonators⁵⁰ and side channels⁵¹ connected to waveguides, while the demonstrated density resonator designs are coated spheres in epoxy¹⁴ and membranes in waveguides⁵⁵.

Several additional resonators designs have been proposed in theoretical negative acoustic index works⁵⁶⁻⁶⁰ and in two recently published experimental papers⁶¹⁻⁶². Focusing on the experimental papers, the metamaterial presented by Zhang et al. consisted of water filled

interconnected chambers in an aluminum plate. Using several limiting assumptions, the chambers and interconnects were modeled as lumped acoustic elements and shown using transmission line analysis to create an experimental sample with positive index in one half and negative index in the other half. A point source located in the positive index region should refocus inside the negative index region, which was experimentally confirmed, but the spot size was diffraction limited indicating evanescent components were not enhanced. Lee et al. presented a negative index design using a combination of membranes and side-holes in a 1-D air filled waveguide. The phase velocity inside a segment of metamaterial was shown to be negative within a band of low audible frequencies in air which the authors attributed to negative index.

Though good first demonstrations, these previously demonstrated negative acoustic index metamaterials have several problems. Zhang's design did not achieve sub-diffraction limit imaging, leaving open the question of whether negative index or only negative refraction was achieved. In addition, the design required rigid walls, which were found in this work to be difficult to attain in water at lower frequencies. The open side holes are the most pressing issue with Lee's design, which can be shown from lumped acoustic analysis to scale improperly when the exit impedance mismatch is included⁶. This limits the design to long wavelengths and low frequencies in air.

In an attempt to overcome the preceding limitations and further the field of negative acoustic index materials, a water-based 2D negative acoustic index metamaterial operating in the 15 kHz - 25 kHz frequency range was designed with the goal of demonstrating a practical negative acoustic index metamaterial. Two resonators were utilized in this design to manipulate bulk modulus and density, HH and rod-spring (RS) resonators. A 1 cm cube of fluid served as the idealized unit cell, maintaining a reasonable scale for conventional machining while remaining sufficiently subwavelength for the effective medium approximation ($\lambda/7.5$ at 20 kHz).

Negative Acoustic Index Physics and Metamaterial Design

From naturally occurring negative properties in electromagnetism and demonstrated negative property EM metamaterials, one can deduce that resonance is the key to achieving negative effective properties in passive materials. Griffiths² demonstrated how dielectric materials can have negative permittivity at resonance, modeling bound electron-core pairs as a mass, the electron, connected by a spring to a fixed anchor, the core. Metals such as silver have nearly free electrons and instead utilize the Drude model, which is equivalent to a simple harmonic oscillator with a natural resonance frequency of zero. As a result, the permittivity dispersion of metals is identical in form to dielectrics, except that the anomalous dispersion is centered at zero frequency⁶³. In both cases, the large electron displacements with significant phase shifts around resonance dominate the average behavior leading to the negative properties.

Since acoustic waves are mechanical waves, mechanical resonators are the obvious choice to manipulate bulk modulus and density and have been utilized in all previously proposed and demonstrated passive negative modulus, density, and acoustic index metamaterials. Active

electromechanical resonators are another option explored later in Chapter 6. Using the definitions in Chapter 1, negative density requires a directional resonator to provide an element accelerating in the opposite direction of an externally applied force, and negative modulus requires an isotropic resonator such that a unit cell on average be expanding when a compressive force is applied⁶⁴. The selected resonators are shown in the negative acoustic index metamaterial unit cell in Figure 4.1 (Left), consisting of a RS resonator highlighted in red to manipulate density and Helmholtz (HH) resonators highlighted in blue to manipulate bulk modulus.

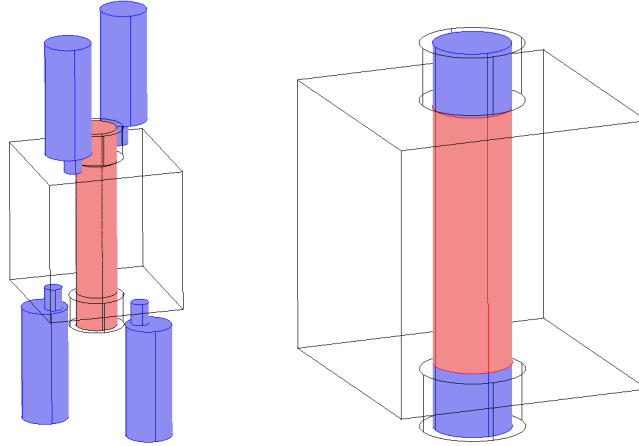


Figure 4.1 Negative acoustic index metamaterial design. (Left) Unit cell consisting of RS resonator in red and four HH resonators in blue, (Right) RS resonator consisting of aluminum mass in red connected to PMMA springs in blue.

HH resonators were selected because they have been previously experimentally shown to achieve negative effective bulk modulus in a 1-D water-filled waveguide acoustic metamaterial⁵⁰. In addition, they are straightforward to fabricate using conventional machining techniques in the frequency range of interest. A negative density elastic metamaterial containing two component mass-spring-damper resonators embedded in an epoxy matrix was the inspiration for RS resonators¹⁴. Initially explained as negative modulus, the authors subsequently published a correct negative density model matching the experimental results⁵². Direct combination of these designs was considered but abandoned due to impedance mismatch and concerns that shear waves supported in the elastic metamaterial could couple with the longitudinal wave of interest. Instead, the RS resonator was created allowing water to replace the epoxy matrix and direct exposure of the mass to the pressure wave.

RS resonators consist of a stiff cylindrical rod acting as the mass and softer material connecting the rod to the waveguide walls acting as springs shown in Figure 4.1 (Right). These springs are hidden in cavities formed in the waveguide walls to minimize their scattering. An estimate of the RS resonance frequency was obtained assuming the deformation was limited to pure shear in the springs and that the spring masses were negligible, resulting in the resonance frequency in Equation 4.1.

$$\omega_{RS} = \sqrt{\frac{Y_s r_s^2}{(1+\nu) h_s h_r \rho_r r_r^2}} \quad (4.1)$$

In Equation 4.1, Y_s is the spring Young's modulus, r_s the spring radius, ν the spring poisson ratio, h_s the spring height, h_r the rod height, ρ_r the rod density, and r_r the rod radius. Equation 4.1 can be derived beginning with the standard harmonic oscillator resonance frequency expression, replacing the mass with the rod mass, and deriving a spring constant from pure shear of a cylinder in the small deformation limit. The actual resonance frequency will be lower due to rod deformations, non-shear spring deformations, and added effective mass from both the viscosity and mass of the surrounding fluid. Simulations and experiments using the final design aluminum rod and PMMA springs indicate the difference can be large, but Equation 4.1 is of the correct order of magnitude. Accounting for the surrounding water mass by adding its density to the rod material density greatly improved the estimate.

HH resonators consist of a fluid filled rigid walled cavity connected by a narrower fluid filled channel called the neck to the surrounding fluid. When the cavity and neck dimensions are all deep subwavelength, HH resonators can be modeled as standard mechanical oscillators with the neck fluid assumed incompressible and serving as the mass and the compressible cavity fluid as the spring. Several HH resonance frequency estimates are available, with one provided in Equation 4.2 for a HH with a flanged neck exit⁶.

$$\omega_{HH} = c \sqrt{\frac{S}{L'V}} \quad (4.2)$$

In Equation 4.2, ω_{HH} is the resonance frequency, c is the fluid phase speed, S the neck cross-section area, V the cavity volume, and L' the effective neck length, defined as the actual length plus 1.7 times the neck radius. This effective neck length accounts for the impedance mismatch at the neck exit. Even with the neck fluid assumed incompressible, the fluid just outside the neck boundaries must flow in and out as the neck fluid moves, creating a complex impedance boundary condition to the lumped neck fluid. For resonance frequency estimations, this is modeled as an additional mass added to the neck fluid mass. Four Helmholtz resonators per unit cell were used in this design in place of the single resonator used by Fang et al. to allow integration with the RS resonators into a well defined unit cell, which is crucial for the RT effective material property extraction routine. Separating the HH resonators into pairs on the top and bottom was done to balance interactions with the RS and to increase symmetry in the vertical direction without creating a preferred lateral direction.

Geometric combination of the HH and RS resonators into a unit cell was straightforward, leaving coupling and loss as issues. A simple analytical relation describing the coupling between the resonators was unavailable, so this was investigated numerically. In the final unit cell design, the individual resonator resonance frequencies did not shift in simulations when combined, and the response amplitudes were only affected a small amount, indicating minimal coupling. Loss, on the other hand, can never be neglected in negative index metamaterials

since the Kramers–Kronig relation can be used to show a large imaginary index component always accompanies resonance in passive materials. As a result, the effective acoustic index of actual passive metamaterials will always be complex, with the imaginary component corresponding to loss in propagating waves and phase changes in evanescent waves, both of which blur and damp the sound pattern. Physically, this large imaginary component is caused by the large particle motions at resonance enhancing the effect of material loss. Mathematically, the complex acoustic index is determined using Equation 4.3.

$$n = \frac{c_0}{c} = \frac{c_0}{|B|} \sqrt{\rho' B' + \rho'' B'' + i(\rho'' B' + \rho' B'')} \quad (4.3)$$

c_0 is the reference phase speed in Equation 4.3. Single primes in Equation 4.3 denote real components and double primes denote imaginary components. This equation reveals another effect of loss, which are the expanded conditions under which a negative real component of acoustic index can be observed as part of a complex refractive index. In these new cases and the original double negative case, the appropriate evaluation of a negative acoustic index material is a comparison of the real and imaginary component magnitudes. Practically, the imaginary component must be sufficiently small relative to the real component for the interesting phenomena accompanying a negative real acoustic index component to be observed. A common criterion is the real component magnitude must at least equal the imaginary component magnitude for a passive metamaterial to be useful.

Negative Acoustic Index Metamaterial Simulations

Simulations using COMSOL Multiphysics version 3.4 with the Acoustics and Solid Mechanics modules and the RT extraction routine described in Chapter 1 were utilized in the design and tuning of HH and RS resonators to achieve negative refractive index. The simulation domain is shown in Figure 4.2. A plane harmonic wave is sent into the domain via the radiation boundary condition at the left boundary towards the unit cell and a zero radiation boundary condition is applied to the right boundary. Radiation conditions allow user defined plane waves to enter the domain while absorbing all plane waves incident on the boundary from the simulation domain. Two lead-in and lead-out segments surround each side of the metamaterial slab, allowing evanescent waves to decay prior to encountering the measurement planes at which pressures are recorded, located between the segments on each side, and the input/output boundaries. The domain side walls are assigned a zero pressure gradient since the structure repeats or is a rigid wall in the transverse directions. RS resonator components are modeled as isotropic elastic solids, while the rest of the domain is modeled as inviscid, isotropic water.

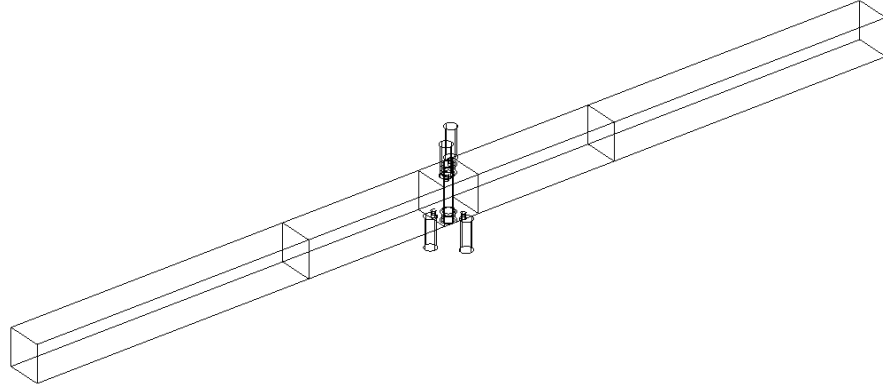


Figure 4.2 Simulation domain with negative index unit cell in center. Plane waves travel from the bottom left boundary towards the top right boundary.

The RS resonators in the best performing negative index combination were composed of a 3 mm diameter, 1 cm long aluminum rod, and 3 mm diameter, 2.5 mm tall PMMA discs. Each RS resonator centerline axis was positioned in the center of a unit cell. The elastic properties assigned to these domains are shown in Table 4.1 along with water properties^{6,65-66}. Since PMMA properties can take a range of values, values were selected within the typical range of hard polymers that resulted in resonance frequencies approximately matching those found in preliminary experiments with samples containing only RS resonators.

Table 4.1 Negative Acoustic Index Material Properties

Material Property	Value
PMMA elastic modulus	4.25 GPa + i*0.15 GPa
PMMA Poisson ratio	0.375
PMMA density	1190 kg/m ³
Aluminum elastic modulus	70 GPa
Aluminum Poisson ratio	0.33
Aluminum density	2700 kg/m ³
Water density	998 kg/m ³
Water sound speed	1481 m/s

Each HH resonator consisted of a neck 1.25 mm in diameter and 1.5 mm long and a cavity 3.4 mm in diameter and 8.5 mm long. The neck center-line axes were 2.5 mm offset in both transverse directions from the RS center-line axis, while the cavity center-line axes were offset 3 mm in both transverse directions from the RS center-line axis. The extra cavity offsets were necessary to provide sufficient material between the HH cavities and spring cavities to accommodate machining errors. Small amounts of loss were added to the neck (8%) and cavity (4%) to mimic viscous losses and the effect of elastic walls. The percentage refers to the imaginary component contribution to the complex phase speed magnitude. For example, a non-dimensional phase speed of $960 + 40i$ is 4% loss.

The real and imaginary effective refractive index components extracted from simulations of the negative acoustic index metamaterial are shown in Figure 4.3, and the corresponding effective bulk modulus and density components are shown in Figure 4.4. The real part of refractive index attains negative values between 19 kHz and 20 kHz, with the real components of bulk modulus and density also negative over this band with the expected resonance shapes. While this metamaterial is double negative, the imaginary index component is greater than the real component in the negative region, demonstrating a poor figure of merit can result even with double negative properties.

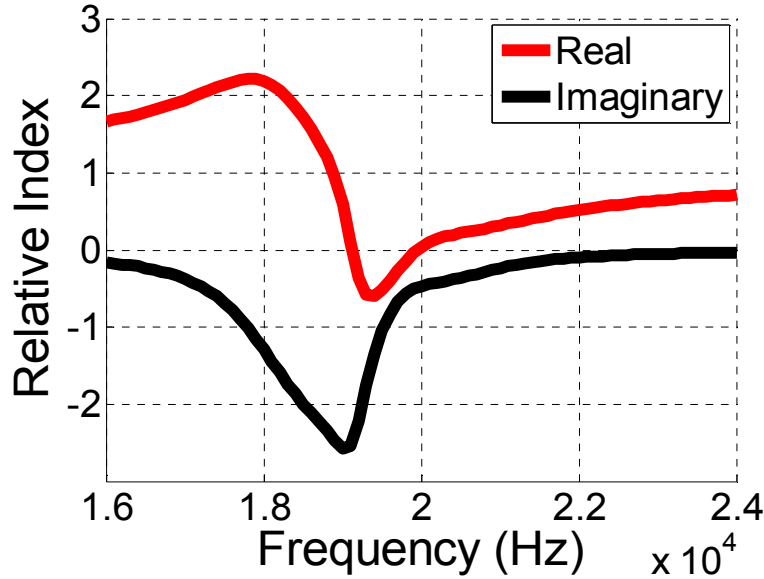


Figure 4.3 Effective refractive index of the negative acoustic index metamaterial unit cell from simulations.

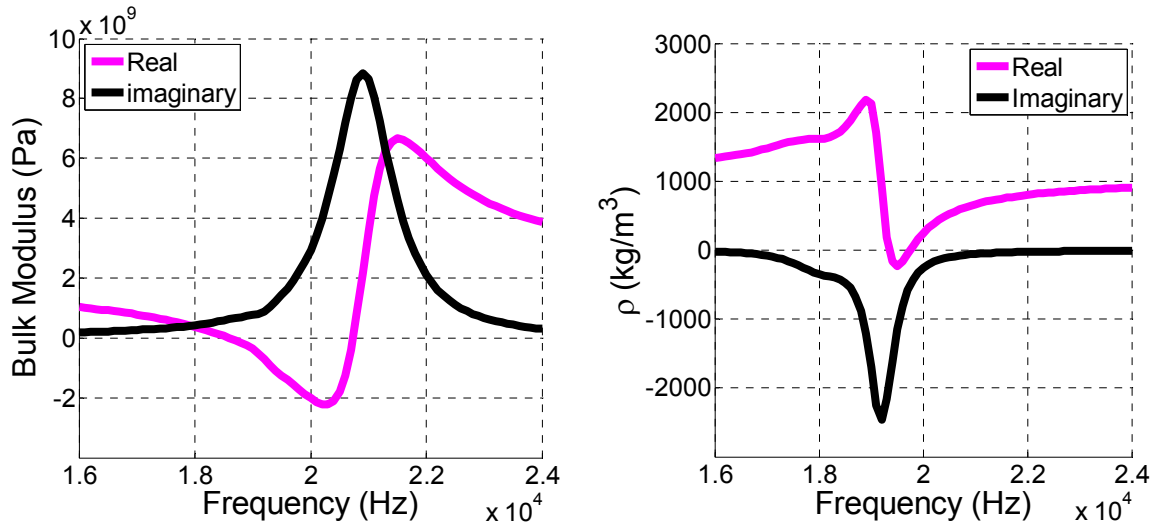


Figure 4.4 Effective (Left) bulk modulus and (Right) density of the negative acoustic index unit cell from simulations.

Further numerical investigations perturbing the geometry and material properties revealed the relative values of the real and imaginary acoustic index components were sensitive to small changes in loss parameters and moderate changes in resonance frequency achieved by geometry modifications. As expected from intuition, decreasing material loss led to greatly improved real/imaginary ratios. Performance also improved as the resonance frequency was increased. This was likely due to the larger size of the resonators relative to the wavelength improving their scattering power. Also, the displacement amplitude required to produce a given pressure amplitude decreases with frequency, reducing the necessary deformation to attain the same effect strength. Of course, actual experimental results were expected to differ regardless due to limitation on the actual experimental sample design, variations in machining quality, actual material properties, and experimental errors, thus making the poor figure of merit that would result from Figure 4.3 unimportant.

Summary

This chapter presented the physics behind negative material properties and previous published work in the effort to create metamaterials with negative acoustic properties. Numerous negative bulk modulus and density metamaterials were identified, as well as two experimental negative acoustic index metamaterials for which the limitations were identified. Theoretical and numerical work was then presented on a 2D negative acoustic index metamaterial utilizing HH and RS resonators to overcome these limitations. This combination attained the desired negative real component of index due to negative density and modulus in simulations. The low ratio of real to imaginary index components was not of great concern since subsequent simulations showed the ratio was highly sensitive to loss parameters and moderately sensitive to resonance frequency, both of which were expected to differ in experiments. With the basic design and detailed geometric parameters specified, experimental implementation was the next step and is presented in the Chapter 5.

Chapter 5 – Negative Acoustic Index Metamaterial Experiments

Introduction

Having established the HH and RS resonator combination as a negative acoustic index metamaterial in Chapter 4, this chapter details the experimental implementation and testing of this combination. Originally, it was planned to test a chain of metamaterial unit cells in a water filled waveguide with a 1 cm x 1 cm cross section that matched the unit cell dimensions. However, testing revealed waveguides were unusable with the available facilities, forcing the use of an alternative sample design and anechoic testing facility. Experimentally determined effective properties using this sample design and setup indicated negative real components of acoustic index and bulk modulus were attained, but insufficient RS performance prevented negative density. The reasons for this are discussed and several solutions outlined as future research directions to overcome these challenges.

Waveguide Setup Testing

Though unnecessary in simulation, real HH resonators require material very rigid relative to the filling fluid in which necks and cavities can be formed. This material is called the structure throughout this chapter. This structure occupies space and would scatter a portion of externally incident waves, making any metamaterial design with HH resonators best suited for use in a waveguide. However, experiments in the 15-25 kHz frequency range on water filled waveguide with reasonable wall thicknesses for the available facilities (around 1 cm) indicated waveguides could not be used. A typical result from pulse experiments is shown in Figure 5.1 (Left), in which a 25 kHz 15 cycle voltage pulse was sent to a source transducer mounted in a waveguide water channel and the pressure signal measured a set distance away using a hydrophone. This specific waveguide was a water-filled 1 cm x 1 cm square cross-section channel with 12 mm thick aluminum walls.

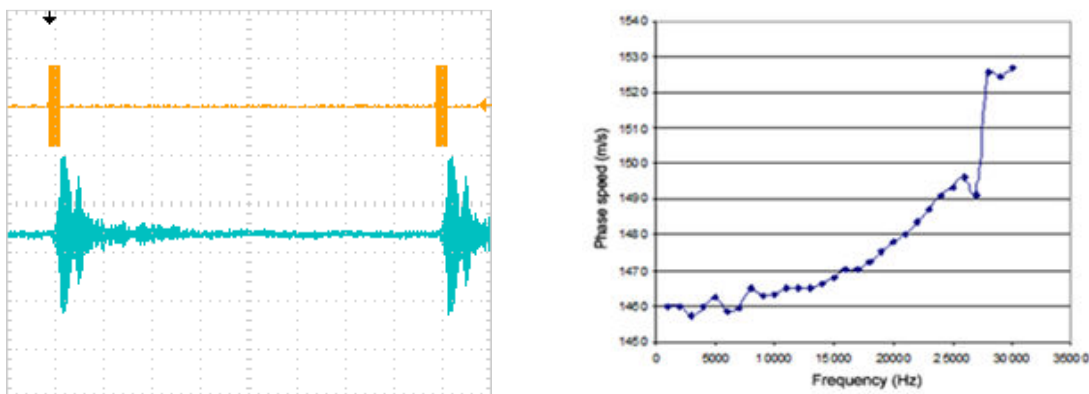


Figure 5.1 Aluminum waveguide pulse experiment results. (Left) Oscilloscope trace of input signal in orange and hydrophone signal in teal at 25 kHz. The first received pulse is the hybrid mode and the second the water mode. (Right) Phase speed of water mode inside the waveguide.

Based on the delay between the driving and received signals, the strong pulse received first traveled at a speed expected of a hybrid mode contained primarily in the metal, while the second weaker pulse traveled approximately the speed of sound in water. These two modes were also clearly identifiable at lower wavelengths using shorter pulses were to avoid pulse overlap. In addition to these undesired modes, the planar fluid zero-cutoff mode was found to be dispersive in the target frequency range as shown in Figure 5.1 (Right). This strong dispersion is a serious problem since it prohibits the use of the RT property extraction method even if the metal hybrid mode was eliminated from the signal through time domain windowing.

Experimental Negative Acoustic Index Metamaterial Design and Setup

Given the inability to use waveguides at the target frequency range, multi-row metamaterial samples were constructed instead and tested in an anechoic chamber. A negative acoustic index version of these samples is shown in Figure 5.2. Six stainless steel bars 1 cm x 1 cm x 11 cm form the structure of a negative index sample, with the HH resonators and pockets for the PMMA discs machined in the center 7cm. Adjacent HH bars were sealed with tape then glued together using marine epoxy. RS resonators were then assembled and attached to the bars using superglue. Finally, to prevent sample breakage, additional 1 cm x 1 cm x 3 cm short bars connected the ends of bars surrounding each row of RS resonators. The resultant samples had 3 rows of 7 unit cells, with a resonator filled cross section of approximately one wavelength in each direction at 20 kHz.

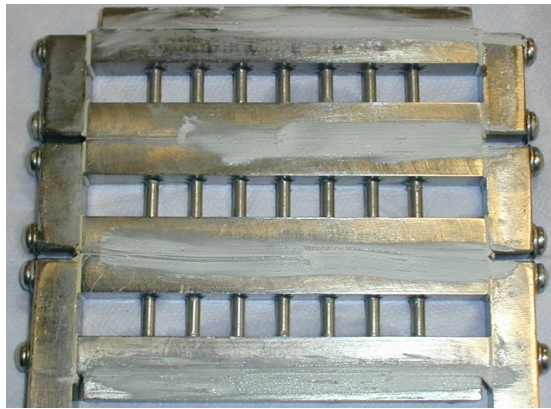


Figure 5.2. Negative acoustic index metamaterial sample. Rods from the RS resonator and the neck openings of HH resonators are visible.

Unlike the originally simulated metamaterial, the unit cell of these samples includes the material in which HH are formed and measures 1 cm x 1 cm x 3 cm. 3 cm is larger than the designated $\lambda/4$ metamaterial cutoff in Chapter 1, but this should not matter for normal incidence provided no coupling or mode conversion occurs in this transverse direction. Effective properties from simulations analogous to those in Chapter 4 of this unit cell modeling the bars as isotropic elastic media were sensitive to boundary conditions, but otherwise indicated a negative real acoustic index component can be attained with frequency dependence similar to Figure 4.3 but decreased tolerance of intrinsic loss.

Reflection and transmission coefficients of acoustic metamaterial samples were measured in a water-filled rectangular anechoic cavity constructed from Syntech Materials Inc. SADM-1 1-1/4 inch thick absorbing panels and 3M Marine Adhesive Sealant, shown in Figure 5.3. The cavity dimensions are roughly 24 cm x 24 cm x 75 cm, which at 20 kHz equates to $3.25\lambda \times 3.25\lambda \times 10.3\lambda$. Pulse-echo measurements indicated reflected wave amplitudes were less than 1/10 the incoming wave amplitude within the frequency range of interest, good anechoic cavity performance. Near-field effects were significant within half a wavelength of the walls, so these regions were avoided during experiments.

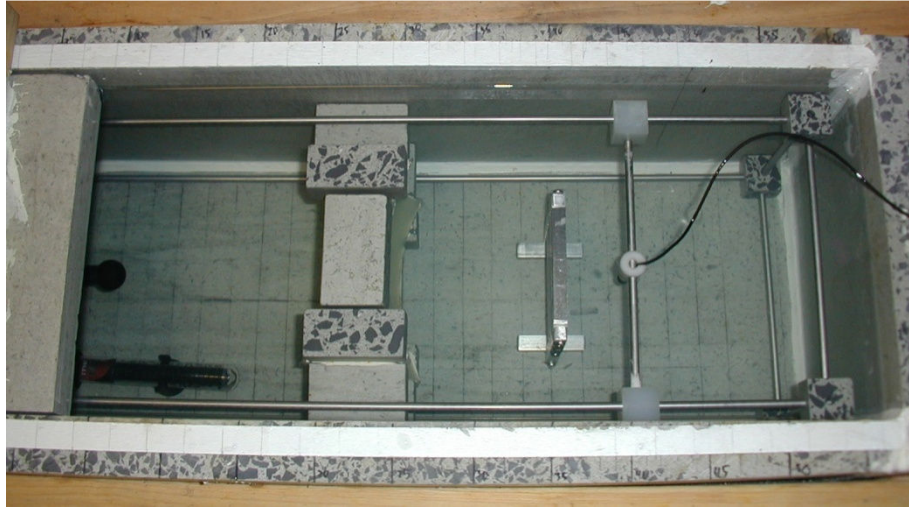


Figure 5.3 Experimental test bay with roof removed. The spherical source and heater can be seen on the left, lens left of center, sample right of center, and receiver on the right of the sample. A rail frame constructed from stainless steel rods and blocks of SADM-1 was used to position the receiving hydrophone in a repeatable manner.

Practical reasons discouraged utilization of a single source large enough to directly create the 15 kHz - 25 kHz plane waves needed to measure RT coefficients for property extraction. Such a source would have to be comparable in size to a wavelength and specially shaped for a specific frequency. In addition, a source this size would strongly scatter any incident waves backscattered from the sample, creating highly undesirable modes between the transducer and sample. Instead, spherical waves from a Reson Inc. TC-4033 spherical transducer driven by a Stanford Research Systems DS345 function generator were collimated by a custom machined Nylon 6/6 lens. The Lensmaker's equation with the thin lens approximation was used to determine the radius of curvature necessary to collimate a spherical source located 25 cm from the lens. Using a phase speed of 2650 m/s for Nylon 6/6 and 1481 m/s for water, the fabricated lens was double-concave with 17.65 cm radii of curvature. Pressure field measurements confirmed a flat phase front beam at least 5cm x 5cm in cross section was created by this setup at frequencies up to 20 kHz. Above 20 kHz distortions in amplitude and phase of the beam rapidly increased.

Local pressure signals were measured using Reson TC-4013 hydrophones mounted on a rail system for positioning accuracy and repeatability. The dimensions of these hydrophones are

deep subwavelength in water at 20 kHz, and measurements using a pair indicated their presence did not perturb the pressure field beyond the adjacent 1-2 mm. Hydrophone signals were passed through a Reson VP2000 amplifier, providing very low noise 50dB power amplification and band pass filtering, and recorded using a Tektronics TDS2004B digital oscilloscope. Recordings were downloaded to a computer for further processing using Matlab® to determine the relative phases and amplitudes for effective property extraction.

Each experiment consisted of measuring the pressure under continuous wave excitation 2 cm in the normal direction from the leading and trailing sample faces, then in the same positions without the sample. At each receiver position, measurements were taken for a set of sufficiently closely spaced frequencies for RT property extraction, with a pause of 3 seconds following each frequency change to allow for steady state. Continuous wave excitation was chosen over pulse mode to eliminate the transients present when changing the excitation of high quality factor resonators, at the cost of increased noise from imperfect absorbing boundary conditions and reflections among the various objects in the chamber creating spurious modes. These noise sources cannot be eliminated by time averaging and were instead reduced by measuring reflection and transmission coefficients with the sample at a five positions in the cavity and averaging the coefficients.

Two experimental parameters that require further comment due to their significant effects on experiments are temperature and sample duration in water. Sample duration in water had two effects. First, air pockets form when a sample is first immersed and filled with water, gradually dissipating with time. A syringe with custom bent needle was used to inject of water directly into the HH cavities and force air out, which decreased the wait time for repeatable results to approximately a day. By continuously storing samples in water except during a quick transfer between a storage tank and the anechoic chamber, this procedure was necessary only once for each sample. Continuous storage in water caused the second effect, which was sample degradation as the superglue holding the RS resonators together gradually failed. Experiments were performed prior to this degradation.

Water temperature during experiments influenced PMMA and water properties, changing HH resonance frequencies slightly and RS resonance frequencies and amplitudes more significantly. The shifts were in opposite directions, with increasing temperature causing the resonance frequencies of the RS resonators to decrease and HH resonators to increase. This dependence was used to fine tune the resonance frequencies, optimizing the overlap of bulk modulus and density effects using the heater in Figure 5.3. Naturally, there were limitations to this tuning method. The maximum usable temperature was 40°C, at which point the water was uncomfortably hot and the adhesives used to assemble the sample and anechoic chamber began rapidly deteriorating. In addition, like most polymers, PMMA material losses increase with temperature. At the high temperature limit the RS resonance frequency was lowest, but the response was also greatly diminished and barely visible in property extractions. Allowing the setup and sample to cool prior to adhesive failure restored the RS response amplitude at higher frequencies.

Experiment Results and Discussion

To ensure the support structure did not cause unexpected resonances, a control sample consisting of the stainless steel bars and side supports without HH or RS resonators was tested first. The transmission coefficient amplitudes with this sample at several positions in the cavity and the average are shown in Figure 5.4. No major resonances appear in the average, indicating anomalous effective properties extracted from subsequent negative index sample measurements were due primarily to HH and RS resonator effects. The limited variation in amplitude was expected for this non-resonant control structure, in which the properties were approximately the volume average and the sample thickness was deep subwavelength over the tested frequency range. The position specific measurements confirm the existence of the minor cavity modes, which are indeed reduced by averaging seen in the black curve.

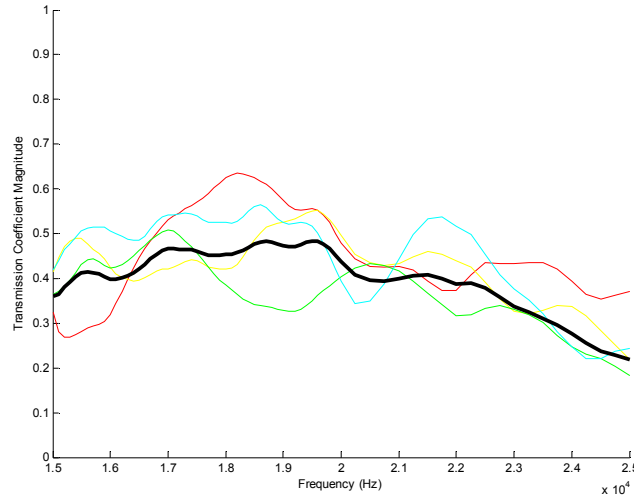


Figure 5.4 Transmission coefficient amplitudes of the control sample. Thin lines denote measurements with the sample at different positions in the cavity, while the thick line is the average of the thin lines.

The effective properties from the best performing negative acoustic index sample are shown in Figures 5.5 and 5.6. The real part of effective index is negative in the frequency band 19-20 kHz, as desired, but a jump occurs above 20 kHz. Below this jump, the refractive index dependence on frequency matches simulations in shape and amplitude except for a small ridge around 17.5 kHz. The resonance induced drops in density and bulk modulus occur over the same band as the negative index, with the curve shapes matching simulation. However, the real part of density is not depressed sufficiently from the volume average to go negative.

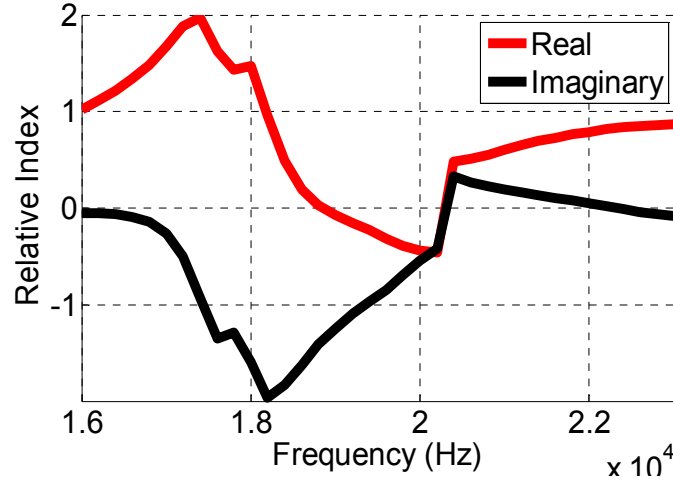


Figure 5.5 Effective acoustic index of the best performing experimental negative acoustic index sample.

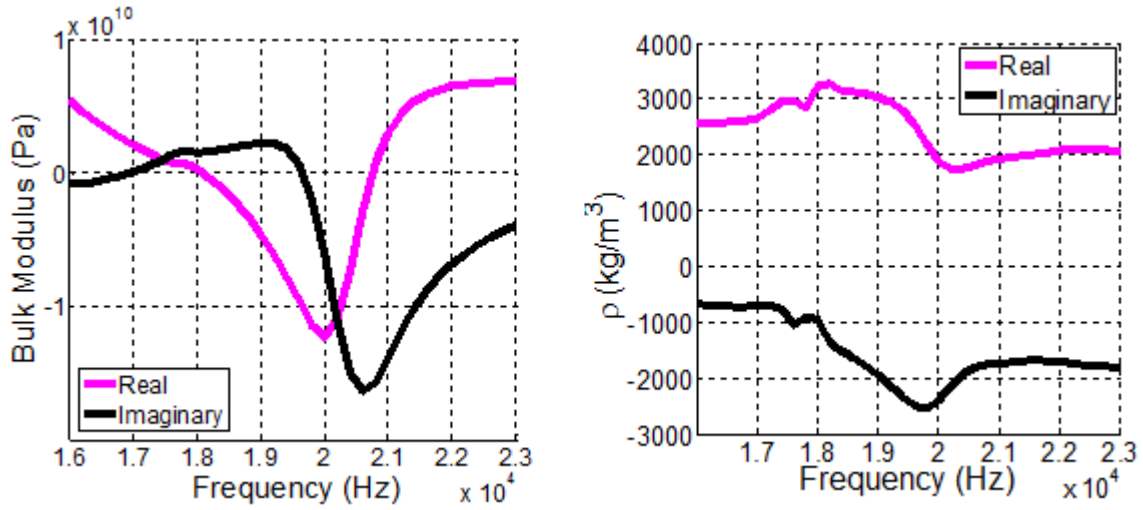


Figure 5.6 Effective (Left) bulk modulus and (Right) density of the best performing experimental negative acoustic index sample.

Although RT property extraction indicates this metamaterial achieved the basic goal of experimentally demonstrating an acoustic metamaterial with a negative real component of acoustic index, several important issues must be addressed beginning with the jump in index just above 20 kHz. This jump was triggered by the RT extraction routine requiring a positive real component of impedance and negative imaginary component of refractive index, which are mandatory for passive metamaterials from energy considerations. However, when one or both of these components is close to zero, as occurred in this case, experimental errors and deviations in assumed parameters cause a solution meeting both requirements to not exist mathematically, at which point the extraction routine fails and attempts to satisfy the impedance condition.

This jump occurred around the same frequency in all experiments that achieved a large negative real component of acoustic index, pointing to systematic errors in the experimental setup or procedures. One obvious error source is the Nylon 6/6 lens performance deterioration at frequencies above 20 kHz. This deterioration was not unexpected, since the quality of the thin lens approximation deteriorates with increasing frequency. In addition, intrinsic loss in the lens increases with frequency since it is composed of a polymer, which affects the rays through the different lens sections varying amounts, distorting the output. Another error source is scattering off other objects in the cavity, which would increase with poor collimation and in general with decreasing wavelength. Finally, the finite sample size creates edge effect distortions including waves refracting around the sample and resonators on the ends of rows responding differently from the bulk due to asymmetric boundary conditions.

Unlike index and impedance, jumps do not occur in bulk modulus or density. Qualitatively, the extracted bulk modulus and density from this sample have the resonant shapes expected from theory and simulation. The HH resonators actually performed better than expected, driving the real part of effective bulk modulus much further negative over a broader band than predicted by the Chapter 4 simulated unit cell, indicating the actual material losses are significantly lower than estimated. This strong response also caused the small resonance shape in density and index around 17.5 kHz, which was repeatable across experiments. Although HH resonators were selected for their strong effect on bulk modulus, they can be shown in simulations to also affect density to a lesser extent at a lower frequency when the intrinsic loss is sufficiently low, as occurred here.

However, unlike the HH resonators, the RS resonators were unable to drive the effective density negative and had a narrower bandwidth than predicted. The lowest real density component extracted from all samples was approximately 1000 kg/m^3 , well short of the necessary decrease to achieve useful negative values. As a result, this single negative metamaterial falls into the same category as the EM negative index metamaterial demonstrated by Shalaev⁶⁷, in which a negative real part of index was achieved with the real component of one constituent property negative and both constituent imaginary components taking large values. While such a design achieves the goal of negative index, the material is not useful given the large imaginary index component relative to the real component.

Weaker amplitudes and a narrower bandwidth point to material loss in the PMMA springs and exposure of the structure in experimental sample design as the two causes of poor RS performance. PMMA was selected due to publications indicating it has low intrinsic loss relative to most polymers⁶⁵⁻⁶⁶. However, polymers properties are typically strongly dependent on frequency, moisture, production methods (extrusion, casting), and temperature, so higher loss levels are not unexpected. Unfortunately, no method to measure the dynamic shear modulus or elastic modulus in the 15-25 kHz frequency range was available to verify this theory at the experimental temperatures, with the available equipment limited to tens of Hz at room temperature. In addition to intrinsic loss, as noted earlier, utilizing a multi-row sample to avoid waveguides increased the performance required of the RS resonators. Exposure of the stainless-steel bars to the incoming waves effectively changed the sample to a composite of

positive and negative materials. Assuming volume averaging is valid at this scale, this requires the RS and HH to respond strongly enough to drive the water channel properties even further negative to overcome the steel bar positive additions to the average.

Future Directions

Based on these HH/RS resonator negative acoustic index metamaterial experimental findings, the major obstacles to attaining useful negative acoustic index are intrinsic loss, narrow bandwidth and the need for a rigid support structure or waveguide. Although the active acoustic metamaterials presented in Chapter 6 can counteract loss and allow active tuning, the only practical method of increasing bandwidth, many applications require passive materials for practical or cost reasons. Two possible methods to meet the loss and support structure challenges in 2D are presented here, with 3D generalization considered in Chapter 6. The first utilizes combinations of coupled resonators and the second utilizes resonators specifically designed for loss tolerance.

Coupling between resonators has the potential to reduce the effects of loss by decreasing local stresses or deformations needed for a given motion, which in turn reduces the effect of intrinsic loss. The starting point for this investigation is the membrane/side-hole negative acoustic index metamaterial noted earlier⁶², which used weakly coupled resonators. This design cannot eliminate the need for a waveguide, but does provide a functioning negative index metamaterial that can be perturbed to provide insight into resonator coupling. Before attempting these perturbations, the negative acoustic index was confirmed via the negative refraction observed in a 3D simulation of the 2D generalization of the original design shown in Figure 5.7.

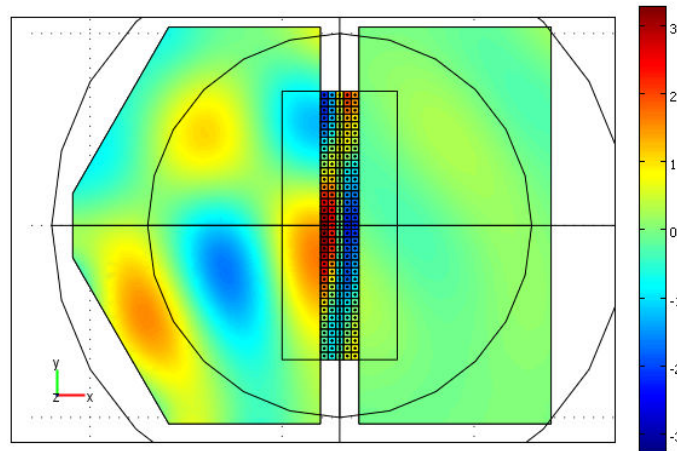


Figure 5.7 Top view of the simulated 2D negative acoustic index metamaterial composed of membrane and side-hole resonators. The source beam enters the domain via the bottom left 30° angled boundary. The inner circle outlines the boundary of a smaller hemisphere serving as open air, while the outer circle is the boundary of the hemispherical absorbing shell.

The metamaterial slab in this simulation is 35 unit cells wide and 5 unit cells thick with the side holes exiting to open air normal to the image towards the reader. Each air chamber is 1.9 cm x 1.9 cm x 2 cm and is separated from adjacent chambers by elastic membranes 1.9 cm x 1 mm x 2 cm in dimension. Perfectly rigid posts 1mm x 1mm x 2cm adjacent to each air chamber corner anchor the membranes. The membranes have a Y of 25MPa, ν of 0.49, ρ of 980 kg/m³, and loss factor of 2.5%. The cylindrical side holes 5 mm in diameter and 5 mm in height connect the chambers to a large hemispherical air domain. An impedance matched hemispherical shell absorbing layer surrounds the air domain, mimicking free space.

With the negative acoustic index of this design established, the first coupling investigation replaced the side holes with HH resonators. HH resonators are appealing due to their functionality over much wider frequencies and fluid choices, ease of tuning, and the elimination of radiation loss. Unfortunately, simulations of HH resonators attached to channels with membranes revealed the coupling actually blocked negative acoustic index. The effect is demonstrated in Figure 5.8, in which effective bulk modulus and density extracted from simulations of the individual elements and the combination are plotted. Membranes alone cause negative density throughout the entire frequency range as seen in the red lines. HH alone cause negative bulk modulus over a frequency band as seen in the green lines. However, combination of the resonators shown in the blue lines radically changed the effective density curve into a typical resonance shape, with the two negative regions excluded from each other.

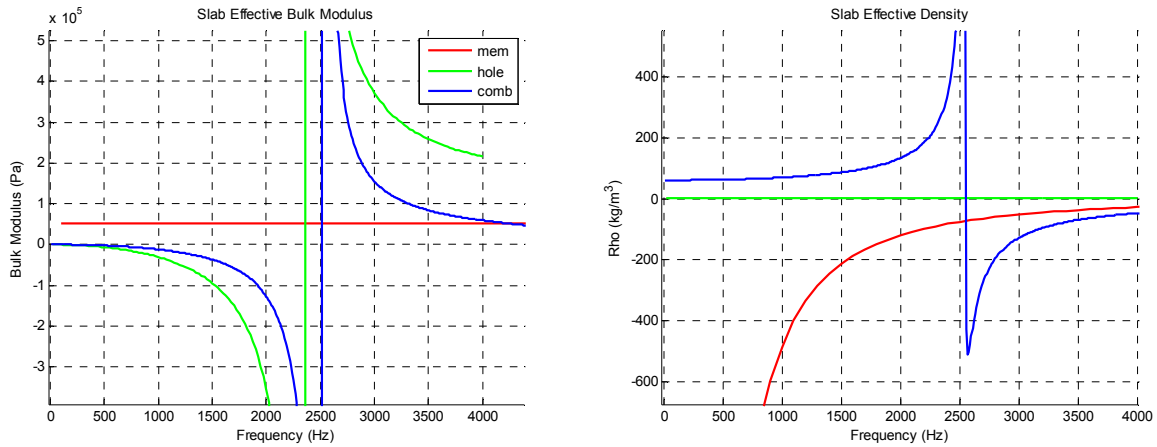


Figure 5.8 Effective bulk modulus (left) and density (right) of metamaterials composed of membranes alone (red), HH resonators alone (green), and the combination (blue).

The next perturbation test changed the filling fluid to water to see if similar membrane and fluid impedances helped. As in the air case, membranes alone attained negative density values at low frequencies, but again the coupling blocked negative acoustic index. Further modifying the membranes by adding cutouts and center masses had mixed results. Cutouts alone shown in Figure 5.9 (Left) greatly reduced the response and eliminated the negative density band, while cutouts with masses shown in Figure 5.9 (Right) showed a weaker negative density band at resonance but greater loss tolerance. However these cutouts eliminated coupling, resulting in a system analogous to the HH and RS resonator combination.

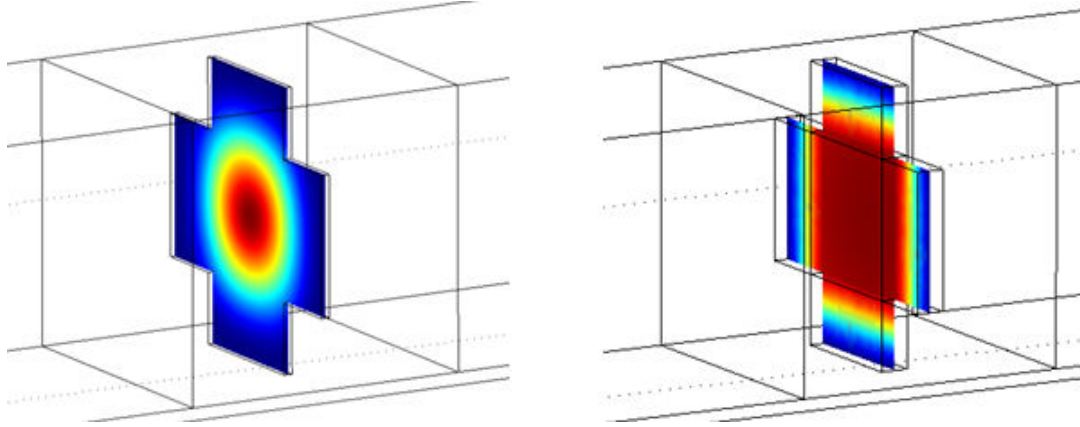


Figure 5.9 Alternative membrane resonator designs. (Left) Membrane with corner cutouts, and (Right) membrane with large square cross-section mass in center and corner cutouts.

In addition to continuing the search for resonator combinations with coupling effects that enhance negative acoustic index, another method of overcoming loss and the need for rigid support structures is using specially designed resonators without consideration of fabrication difficulty. Given the success of HH resonators in driving bulk modulus negative and the ability to generalize them to 2D, here the focus was on developing a loss tolerant density resonator. This resonator is shown in Figure 5.10 (Left) under maximum deformation in a 2D simulation. The resonator consists of a 3 mm diameter lead rod connected to an aluminum shell 0.5 mm thick with an outer diameter of 5 mm via polymer or metal fins. In this specific design the fins are 50 μm thick and composed of lead.

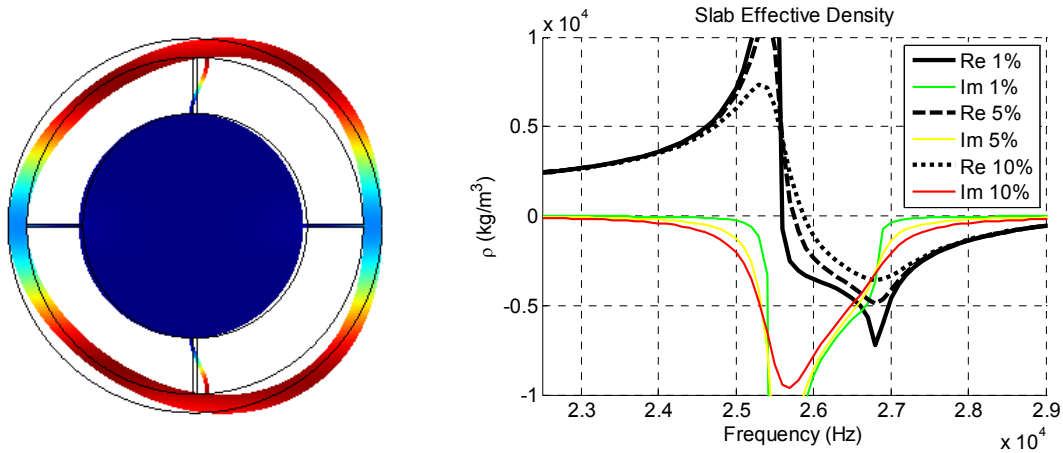


Figure 5.10 New negative density resonator. (Left) Simulation of unit cell with deformed shape plotted in color. (Right) Effective density as a function of frequency for various polymer fin loss levels. The Re and Im refer to real and imaginary density components, and the percentage to the loss factor magnitude.

As with the RS resonators, this design can be modeled as a mass-spring-damper resonator. The key is to make the core significantly more massive than the shell and fins. This reduces the

mass-spring-mass system formed by the shell-fins-core to a mass-spring system formed by the shell-fins, since the core displacement will always be much smaller than the shell displacement under sufficiently high frequency harmonic excitation. This also allows the core to serve as an inertial anchor, eliminating the need for an external rigid structure. A soft support structure is needed only to hold the resonators in an evenly distributed array.

Increased tolerance of intrinsic loss is accomplished by using fins instead of a solid coating. This reduces the total volumetric deformation needed in the springs to displace the mass and allowed use of lower loss materials as the springs. Large loss tolerance results as shown in Figure 5.10 (Right), where the effective densities have significant negative regions even with high loss factors of 10%. Negative density with slightly lower loss tolerance was also found using polymer fins 250 μm thick and in designs using square cross-section cores and shells, both of which may be preferable for fabrication purposes. Of course, resonator coupling, geometric arrangement, and fabrication/experimental challenges remain to be resolved before this design can be seriously considered.

Summary

This chapter presented the experimental implementation of the negative acoustic index metamaterial design from Chapter 4 and the best set of extracted effective properties. The combination of HH and RS resonators was found to attain a negative real component of index, but instead of being a double negative metamaterial, the cause was a large negative real component of bulk modulus and large imaginary bulk modulus and density components. The inability of the RS resonators to drive the real part effective density negative was likely due to PMMA loss and the increased resonator demands imposed by design changes. As a result of this failure, the imaginary acoustic index component magnitude exceeded the real component magnitude over the negative band.

While this acoustic metamaterial did not satisfy the goal of creating a practical negative acoustic index metamaterial, the information gained is being used in several ongoing efforts to both improve this design and develop alternatives. First, improved experimental setups and samples are clearly needed to conclusively evaluate the HH/RS resonator combination. To this end, a larger sample for testing in the higher quality facilities at the Naval Research Labs is in progress. Second, alternative resonators using coupling and specially designed resonators tolerant of loss were investigated and shown in this chapter to offer possible solutions to the current problems. Finally, loss will be an issue in all passive negative property metamaterials. Active elements have been investigated to directly overcome the loss, with the work presented in Chapter 6.

Chapter 6 – 3D and Active Acoustic Metamaterials

Introduction

The preceding chapters in this dissertation have focused on proof of concept demonstrations, in which 1D and 2D systems have been analyzed and tested under simplified conditions. Naturally, for acoustic metamaterials to reach their true potential these systems must be generalized to 3D and in the case of negative property metamaterials, will likely need to utilize active elements. This chapter presents numerical investigations into 3D generalizations of the cylindrical hyperlens, resonators for a 3D negative acoustic index metamaterial, and the ability of active elements to provide user selected material properties including gain. While numerous practical challenges must be resolved in each of these designs, they provide a starting point for future acoustic metamaterial research towards the next major steps in each field.

3D Acoustic Hyperlens

Generalization of a 2D hyperlens design to 3D is straightforward in acoustics because the velocity fields of the acoustic waves are longitudinally polarized. The 3D generalization of the 2D cylindrical design is a hemispherical solid brass shell perforated by tapered air filled holes in the radial direction as shown in Figure 6.1 (Left). 869 tapered holes expand from 1 mm at the shell inner radius of 3 cm to 8mm at the outer radius of 24cm, providing 8 times magnification analogous to the 2D case. Computational power limitations restricted simulations of this design to the infinite density contrast case and only the holes within 30 degrees of the vertical direction shown in Figure 6.1 (Right). Perfectly matched absorbing layers were used to prevent boundary reflections. As in the 2D case, the sound pattern from two circular speakers originally $\lambda/5.7$ in diameter is successfully magnified at 5 kHz into propagating beams, with the hyperlens maintaining broadband performance similar to the 2D case.

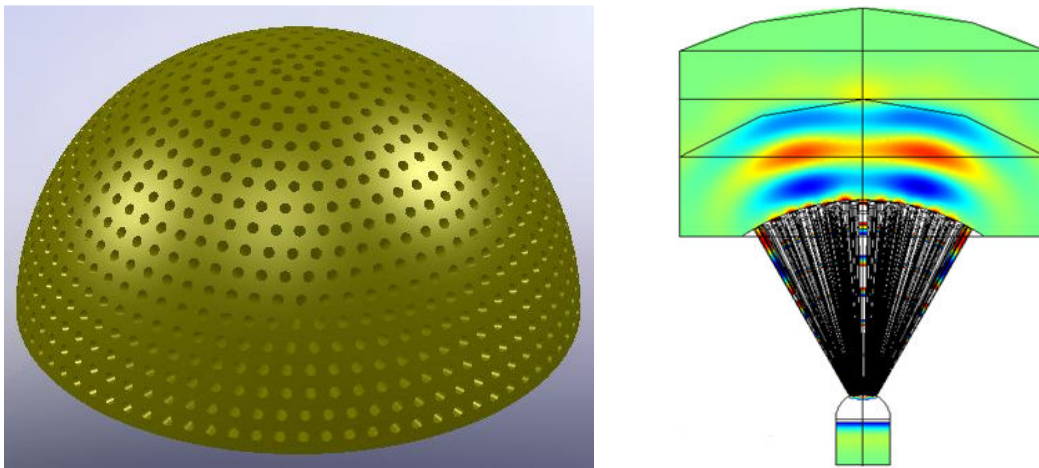


Figure 6.1 3D spherical hyperlens. (Left) Solid model of hyperlens created in Solidworks®, (Right) Comsol® simulation at 5 kHz showing magnification of $\lambda/5.7$ disc speakers.

As one might expect for this and all curved 3D structures, the challenge in this design is devising a fabrication method, much less a cost-effective method. Based off conversations with a specialty CNC machine shop, conventional machining of a one piece hyperlens has been ruled out due to the difficulty in creating tapered holes with aspect ratios this large. It may be possible to fabricate the design using the cascaded layer design mentioned in Chapter 5 for increased magnification, but this would be extremely costly due to the number of layers required. Currently, the method identified as most likely to succeed is using sterolithography or another rapid 3D prototyping technique to create a plastic 3D hyperlens. Preliminary 2D simulations into imaging using a hyperlens formed from thin, discrete layers indicate such a hyperlens still has high enough density contrast to function in air, with the effects of discrete layers dependent on the layer thicknesses. Using the minimum thickness for rapid prototyping would create an excessively long fabrication time, but simulations show discrete layers of such thickness do not noticeably affect hyperlens performance compared to the smooth wall case.

3D Negative Acoustic Index Resonators

To transition negative acoustic index metamaterials from 2D to 3D, new resonators are needed for bulk modulus and density. In the case of bulk modulus, the experimentally demonstrated HH resonators and side-hole designs require rigid waveguide structures and cannot be generalized to 3D. However, the ideal resonators for negative bulk modulus actually already exist in nature and engineered materials. Bubbles and gas filled coated spheres common in ultrasonic imaging are deep subwavelength at the resonance frequency of the spherically symmetric mode matching negative bulk modulus, and also do not need hard support structures. These have been avoided in the past due to difficulty in anchoring an array without significantly perturbing the system, with bubbles having the additional challenge of size control. Based off discussions with the Naval Research Labs in Washington D.C., it is believed that a gel matrix can resolve these problems and allow a bubble array to attain negative bulk modulus. A method has been developed there to form bubble arrays inside a gel matrix with tight size distribution and good stability over time. Further research is needed on the influence shear modes, material compatibility, and impedance mismatches, but the end result could be the ideal 3D negative bulk modulus metamaterial.

No ideal negative density resonator design exists in nature to pair with bubbles, so a 3D mass-spring-damper design was developed along the same lines as the 2D loss tolerant design presented in Chapter 5. This resonator is shown in a 1 cm water filled cubic unit cell in Figure 6.2 (Left), with color slice plots of the elastic media displacement highlighting the core, fins, and shell. The inertial core is a 3 mm cube of lead and the cubic shell is composed of 0.5 mm thick aluminum with outer edge lengths of 5 mm. Lead fins 750 μm long with 250 μm x 250 μm square cross-sections extend from the center of each core face to the center of each shell internal face. In these simulations, the space between the core and shell not occupied by the fins was modeled as vacuum, but air should not noticeably change the results. Mechanical properties assigned to these regions were textbook values⁶.

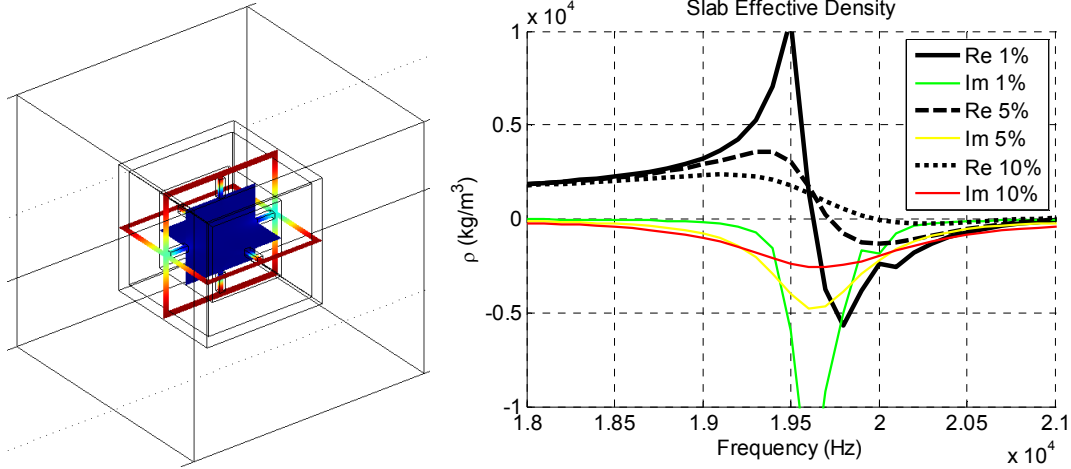


Figure 6.2 3D negative density resonator. (Left) Simulation unit cell with displacement plotted in color slices. (Right) Effective density as a function of frequency for various loss factors.

Using the same principles as the 2D case in Chapter 5, this resonator can be modeled as a mass-spring-damper system due to the core mass greatly exceeding the shell mass, which again eliminates the need for a rigid external structure. Overcoming intrinsic loss sensitivity was accomplished again by using fins instead of a solid coating, resulting in significant loss tolerance as shown in Figure 6.2 (Right). While less than that achieved in the 2D case, loss factors up to at least 5% result in negative density bands with extended regions where the negative real component amplitude exceeds the imaginary component amplitude. The extra feature visible just below 20 kHz in the 1% loss factor curves are due to an additional loss-sensitive mode in this design. Anisotropic response is a legitimate concern in the cubic resonator design and was tested by rotating the resonator 45 degrees as shown in Figure 6.3 (Left). The resultant effective density shown in Figure 6.3 (Right) is slightly phase shifted indicating minor anisotropy, but is otherwise identical.

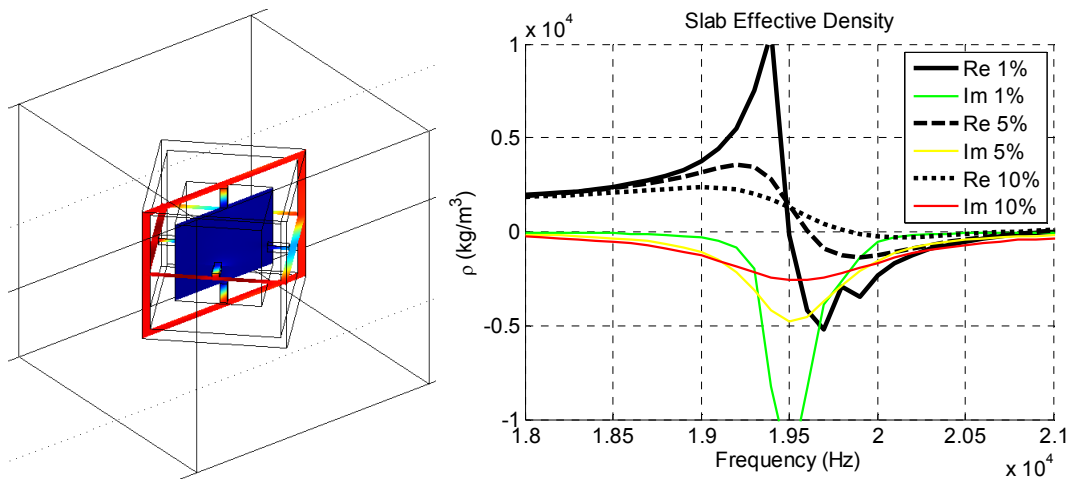


Figure 6.3 Rotated 3D negative density resonator. (Left) Simulation unit cell with displacement plotted in color slices. (Right) Effective density for various loss factor amounts.

Cubes were chosen in the 3D design based off the understanding that they are easier to fabricate than spherical structures. A resonator composed of a spherical core connected by six pin fins to the surrounding spherical shell was also simulated and found to have similar performance, but lower loss tolerance. Regardless of the shape choice, the next steps in the development of this negative acoustic index material are to investigate the effects of a gel matrix on wave propagation without bubbles and these new density resonators. If the results are encouraging for the longitudinal modes of interest, resonator arrangement and coupling should be studied next, with resolution of fabrication and experimental challenges the final steps.

Active Acoustic Metamaterials Background

From the experimental results in Chapter 5 and from experimentally demonstrated EM negative index metamaterials, it is apparent that the most pressing problems plaguing all passive metamaterials with negative properties are intrinsic loss and narrow bandwidths. Although creative EM designs⁶⁸ have been able to greatly decrease these effects under restrictive conditions, the only way to fully overcome them is to use active elements. In the acoustics work here, two active element implementations were investigated. First, the ability of elements to directly combat amplitude decay by injecting energy coherently with the passing waves was tested. In this scenario, the active “gain” elements would be used in conjunction with the passive bulk modulus and density resonators. Second, the ability of active elements to completely replace the original negative property resonators was tested. This implementation potentially allows both gain through coherent energy injection and active tuning to increase the bandwidth of negative regions, but will be considerably more complicated to implement.

Before delving into the numerical investigations done here, it is important to understand the different physics behind gain in active acoustic metamaterials and active EM materials. Gain in EM materials is a mature field, with gain materials widely used in common commercial devices like lasers and in experimental research systems like plasmonic waveguides⁶⁹. These materials amplify waves using the stimulated emission process, which occurs when an inverted population of electron energy states is created in an active material by EM pumping. Passing wave quanta of the appropriate energy stimulate some of the excited particles to relax to a lower state, releasing additional coherent quanta that amplify the wave. The critical point here is the coherence of the released quanta with the passing quanta is due to a quantum mechanical effect, not the pumping wave characteristics.

Unfortunately, acoustic gain materials at the length and temperature scales of interest here cannot directly mimic this method. Fundamentally, stimulated emission is a quantum mechanical effect and in Hz-MHz frequency range at room temperature quantum mechanical effects are completely negligible in mechanical waves. One must go to ultra-high GHz-THz frequencies in single nanometer scale lattices at near zero Kelvin temperatures such as in the work by Walker et al.⁷⁰ to make quantum effects observable in mechanical wave systems and stimulated phonon emission possible. The key features of commonly used acoustic waves that allow effective gain without quantum effects are much slower speeds and much lower

frequencies relative to EM waves. With the GHz processing speeds and MHz switching speeds available today, the amplitude and phase of active acoustic elements relative to the passing fields can be directly engineered instead of relying on quantum effects. The challenge is to properly program an array of deep subwavelength active acoustic elements to detect the externally applied field and use external energy to generate additional acoustic waves with the appropriate phase and amplitude relations.

The 2D active acoustic metamaterial unit cell utilized the both of the numerical studies performed in this chapter is shown in Figure 6.4. A 1 cm x 1 cm water filled square forms the core of the unit cell. Two piezoelectric lead-zirconate-titanate (PZT) transducers 3 mm x 2 mm were positioned symmetrically in cavities at the top and bottom of the water core, with the inward exposed surfaces flush with the core. These inward exposed surfaces were mechanically coupled to the fluid through a normal force balance and electrically driven at the same frequency as the incoming wave, while the opposite surfaces were rigidly fixed and electrically grounded. The electromechanical properties assigned to the PZT were the default COMSOL properties shown in Equations 6.1-6.3, suitable for a hard PZT. In these equations, S_E is the elastic compliance, d is the piezoelectric charge constant, and $\varepsilon/\varepsilon_0$ is the permittivity relative to that of free space.

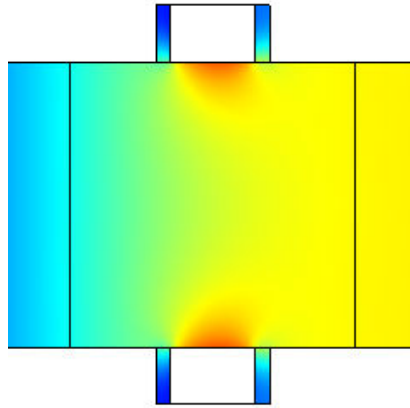


Figure 6.4 Pressure field snapshot of active acoustic metamaterial unit composed of a water core and two symmetric flush mounted piezoelectric elements (white rectangles) sandwiched between water filled waveguides.

$$S_E = \begin{bmatrix} 16.5 & -4.78 & -8.45 & 0 & 0 & 0 \\ -4.78 & 16.5 & -8.45 & 0 & 0 & 0 \\ -8.45 & -8.45 & 20.7 & 0 & 0 & 0 \\ 0 & 0 & 0 & 43.5 & 0 & 0 \\ 0 & 0 & 0 & 0 & 43.5 & 0 \\ 0 & 0 & 0 & 0 & 0 & 42.6 \end{bmatrix} \times 10^{-12} \frac{1}{Pa} \quad (6.1)$$

$$d = \begin{bmatrix} 0 & 0 & 0 & 0 & 741 & 0 \\ 0 & 0 & 0 & 741 & 0 & 0 \\ -274 & -274 & 593 & 0 & 0 & 0 \end{bmatrix} \times 10^{-12} \frac{C}{N} \quad (6.2)$$

$$\frac{\epsilon}{\epsilon_0} = \begin{bmatrix} 3130 & 0 & 0 \\ 0 & 3130 & 0 \\ 0 & 0 & 3400 \end{bmatrix} \quad (6.3)$$

Active Acoustic Metamaterials Investigations

The specific question concerning gain in active acoustic metamaterials investigated here was whether deep subwavelength transducers can output sufficient energy at reasonable voltages to achieve significant amplification. Basic acoustic transducer theory states the amount of energy output by a transducer is proportional to its characteristic length squared⁶. This creates a potential problem since effective medium theory places a limit on the maximum permissible element size for a given wavelength and requires elements be as small as possible, while basic transducer theory indicates shrinking transducers will cause the gain per transducer to decrease faster than the packing fraction per wavelength increases.

To answer this question, the PZT elements in the active acoustic metamaterial unit cell were driven by an oscillating 0.01 V electric potential boundary condition $\pi/2$ radians ahead in phase of the 1 Pa incident wave phase at the unit cell center over the 0-20 kHz frequency range (1 cm equals $\lambda/7.5$ at 20 kHz). This phase shift should actually change slightly with frequency for optimum results due to the large but finite mechanical impedance mismatch between PZT and water, but from phase tuning in simulations it was found that the improvements will be minimal. The resultant real and imaginary effective index components relative to water are shown in Figure 6.5, where a positive imaginary index component signifies gain.

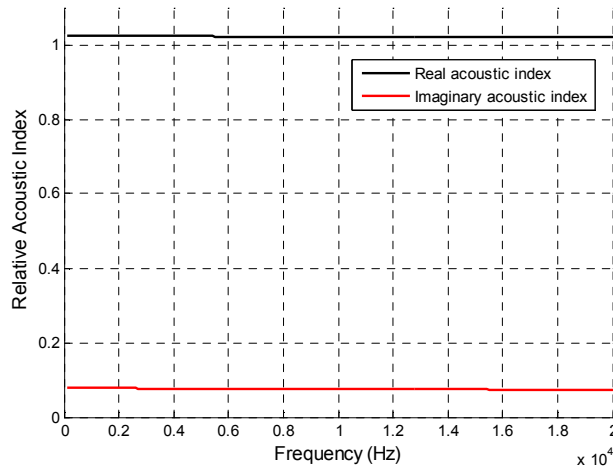


Figure 6.5 Effective acoustic index of the active acoustic gain metamaterial with piezoelectric elements driven at 0.01V acting on a 1 Pa incoming wave.

The RT extraction routine of Chapter 1 was used to obtain these properties, except the requirements of positive imaginary index components and positive real impedance components were removed. Instead, the applied voltage was restricted to low values to keep the active elements weak. This allowed constraints of positive real components of acoustic index and impedance to be applied, since a small perturbation should leave these values near their unperturbed values, which are strongly positive. The observed imaginary index component of approximately 0.08 compared to the real index component of approximately 1 is respectable for the small applied voltage. However, it must be remembered that, unlike in stimulated emission, the energy added does not automatically scale with the incoming wave amplitude. The driving voltage must also be increased to add a proportional amount of energy to higher amplitude waves.

Increasing the voltage and incident pressure proportionally up to a driving voltage of 10 V and incident pressure wave amplitude of 1000 Pa resulted in effective acoustic index curves identical to those in Figure 6.2 within numerical error. While this linear scaling is helpful in terms of developing control routines for the active elements, it also makes apparent the limitation on practically achievable gain. 10 V is approximate the limit of modern portable energy systems, meaning the maximum amplitude pressure wave in water that can be amplified reasonably fast is only 1000 Pa, which is weak by water acoustics standards. If higher gain levels are required, this further reduces the allowable incident wave amplitude.

Although these findings could be interpreted as discouraging, it must be remembered that not all applications require strong amplitude waves or will operate in water. Imaging in particular only requires that signals sufficiently exceed the noise level after processing, which can be very low. This study shows active piezoelectric elements of a given size can provide significant gain up to a certain frequency and amplitude. Use of effective medium theory sets the upper frequency limit above which a unit cell can no longer be considered an effective medium. Practical voltage constraints limit the maximum rate of energy injected into the system, which in turn limits the maximum amplitude incident wave for which significant gain can be attained. The specific limit can be increased through improved active element design or material choice but can never be eliminated.

Before presenting the numerical investigations on replacement of resonators with active elements done here, it should be pointed out that theoretical works on active acoustic elements that replace passive resonators have very recently been published by another group⁷¹⁻⁷³. Noting that the negative density found using membranes and negative bulk modulus found using HH resonators were restricted to limited frequency bands, the authors replaced membranes with piezoelectric diaphragms and HH with wall mounted piezoelectric elements to see if broadband performance could be attained. Modeling these elements as additional electric circuits in a lumped acoustic transmission line analysis converted to the electric analog, the authors were able to derive the necessary driving voltage amplitudes and phases as a function of frequency to result in a target negative bulk modulus or density.

The quantitative results from these studies are encouraging, with low driving voltages over the tested frequency range except at very low frequencies and the use of active elements as self sensors. However, there are limitations to these works due to the use of lumped analysis, which contains hidden assumptions concerning the deformation and radiation patterns of the active elements. The study presented here sought to answer the question of whether broadband bulk modulus control could be achieved using the active acoustic metamaterial unit cell using full wave simulations without the lumped assumption. Ideally one would like to immediately test whether a broadband of negative, real bulk modulus can be maintained at reasonable driving voltages, but the RT extraction routine could not be made sufficiently robust without the passive material restrictions on the signs of imaginary index and real impedance components.

To get around this, first the phase of a 0.01 V driving voltage relative to a 1 Pa incident wave was incremented by $\pi/8$ size steps to see if an optimum phase existed to drive bulk modulus down from the volume average. The resultant bulk modulus and density curves for all 16 phases are shown in Figure 6.6. None of the lines cross in either of these plots. Two points were observed from these figures. First, an optimum phase does exist, which in this case was zero phase difference between the driving voltage and incident wave phase at the unit cell center. This means the peak pressure of the incident wave and peak PZT driving voltage occur at the same time in the unit cell. Second, the density is virtually unaffected by this unit cell design, which was expected given the isotropy of the field radiated by the active elements relative to the wave propagation direction.

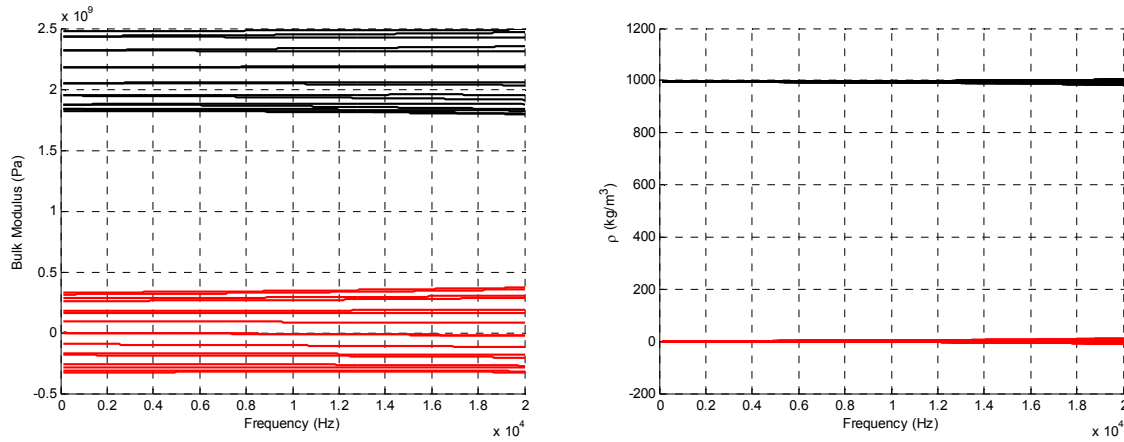


Figure 6.6 Effective (Left) bulk modulus and (Right) density of the active acoustic metamaterial unit cell driven at 0.01 V with various phases relative to the incident wave. Real components are plotted in black and imaginary components in red.

With the optimum phase at this driving voltage identified, the driving voltage was gradually increased while keeping the phase constant to increase the effect on bulk modulus. This provided the RT extraction routine a way to select the correct index and impedance. Each voltage increase can be considered a perturbation of the previous level, allowing selection of the appropriate solution based off the smallest change relative to the previous solution. The

resultant bulk modulus for driving voltages from 0.01 V to 0.2 V by 0.01 V steps are shown in Figure 6.7 (Left). The highest real and imaginary component curves correspond to the 0.01 V driving voltage, with each step up in driving voltage corresponding to the next curves down.

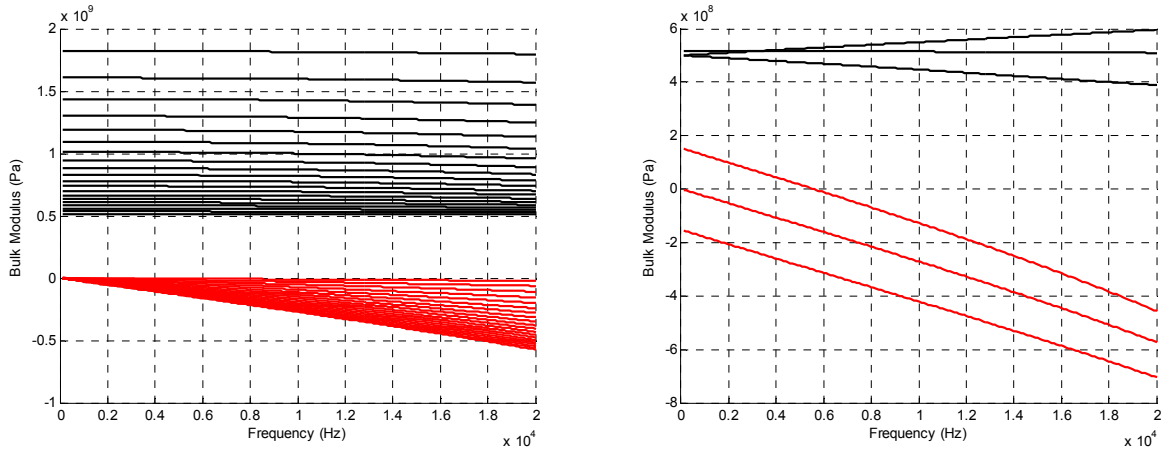


Figure 6.7 Effective bulk modulus of the active acoustic metamaterial unit cell for (Left) zero phase and increasing driving voltages and (Right) constant 0.2 V amplitude and $\pi/8$ phase shifts from zero phase. Real components are in black and imaginary components in red.

From Figure 6.7 (Left), it appears increasing the driving voltage from the voltage/phase combination that resulted in the largest bulk modulus decrease at 0.01 V does not eventually drive modulus negative. Although initially promising, the magnitude of additional decreases in bulk modulus declines with increasing driving voltage, leading to an eventual plateau for practical frequencies. Varying the phase by $\pi/8$ about zero in both directions at the 0.2 V driving voltage amplitude did not significantly improve the situation, as shown in the curves of Figure 6.7 (Right). Having the driving voltage lead the incident pressure wave created a downward trend in the real part of bulk modulus, but it will not reach negative values before the effective medium theory frequency cutoff. At this point it is clear active elements can maintain broadband bulk modulus values below the volume average, but it is unknown whether broadband negative values can be maintained. More work is needed to resolve this issue.

Summary

This chapter presented numerical work on the 3D extensions of acoustic hyperlens and negative acoustic index, as well as investigations into the potential for active acoustic metamaterials to overcome the intrinsic loss and narrow bandwidth hindering current negative property acoustic metamaterials. Generalization of 2D acoustic hyperlens to 3D was shown to be straightforward in theory, with idealized simulations indicating the sub-diffraction limit magnification capabilities were unchanged by the switch. Changing from 2D to 3D negative acoustic index metamaterials was considerably more challenging, with new resonators needed for both bulk modulus and density that do not require waveguides or rigid structures. A

combination of bubbles or coated gas spheres as bulk modulus resonators and a cubic 3D mass-spring-damper density resonator was proposed, with the density resonator shown to tolerate reasonable amounts of loss.

The studies on active acoustic metamaterials indicated much work remains to be done in this field. Significant gain was found to be possible in a water-based acoustic metamaterials using piezoelectric elements, with the output power scaling linearly with voltage. Practical voltage constraints created the upper limit to the maximum amplitude of an incident wave that can be amplified within a reasonable distance. The study on increasing the bandwidth of anomalous bulk modulus values concluded a broad band of values depressed from the volume average can be maintained, but was inconclusive as to whether negative values could be obtained or held over a broad frequency band at reasonable voltages. It should be pointed out that neither of these studies addressed technical issues such as sensing the incoming wave or maintaining a stable control loop. These problems must be resolved on a case-by-case basis once the desired gain and broadband response of a design has been verified as possible.

Chapter 7 – Conclusions and Outlook

Conclusions

The preceding chapters in this dissertation covered theoretical and experimental work on anisotropic acoustic metamaterials, negative acoustic index metamaterials, and active acoustic metamaterials. Development of anisotropic acoustic metamaterials was motivated by the possibility of far-field imaging of sub-diffraction limit sound patterns using the hyperlens method first demonstrated in EM. This method was shown to require high density anisotropy in fluid acoustics, which was attained theoretically and numerically in an asymmetric air-brass layered microstructure. Experimental results using a 2D cylindrical acoustic hyperlens composed of this metamaterial showed successful 8 times magnification of sub-diffraction limit speaker arrangements resulting in clearly separated sources in the far-field. Further detailed analysis of the amplitude and phase along a beam provided additional evidence of the successful conversion of evanescent information to propagating waves, and microstructured simulations were shown to support the validity of modeling the metamaterial as a fluid.

The pursuit of negative acoustic index metamaterials focused on a fluid metamaterial design combining HH and RS resonators to manipulate bulk modulus and density, respectively. Following simulation results confirming the combination generated negative real components of bulk modulus and density resulting in a negative real acoustic index component, experimental challenges and solutions were detailed, culminating in experimental results showing attainment of a negative real component of acoustic index. A detailed examination of the negative acoustic index revealed it was caused by a negative real component of bulk modulus and large imaginary components of bulk modulus and density, resulting in large loss that limits the potential applications of this material to band damping. Besides the possibility of experimental errors affecting the results, intrinsic loss and the inability to use waveguides were identified as the primary culprits preventing the success of this resonator combination.

Since the use of active acoustic elements is the only currently known method to fully overcome the intrinsic loss and narrow bandwidth in negative acoustic property metamaterials, numerical work was done to evaluate the capabilities of active piezoelectric elements to generate gain and negative bulk modulus. Using a simple 2D water-filled unit cell with two symmetric PZT active elements, significant wave amplification was verified to be possible for sufficiently low amplitude incoming waves up to the effective medium cutoff frequency. However, only depressed bulk modulus, not negative bulk modulus, was found to be possible using a simple tuning method developed and utilized here. Further perturbations on the driving phase indicated a driving phase that varies with frequency will be required to reach negative values.

Outlook

As indicated by the extensive references and the work presented in this dissertation, the field of acoustic metamaterials is currently undergoing rapid growth as the homogenization of man-made microstructures and frequency dependence of acoustic properties at commonly encountered frequencies are gaining widespread acceptance. In addition to the continuing

research into solving the challenging problems of intrinsic loss and resonator design, many other types of mechanical waves have yet to be investigated from the metamaterial perspective, including Rayleigh, Lamb, and shock waves. These fields are ripe for application of metamaterial theory with the same potential to for novel phenomena and applications that inspired electromagnetic metamaterials.

Specific to the acoustic hyperlens project, the work presented in Chapters 2 and 3 completed a proof-of-concept of the acoustic hyperlens imaging, leaving future research in this field focused on extending the design capabilities to allow transfer of the device from a research setting to industry. Preliminary numerical investigations into increasing magnifying power and changing to flat input/output interfaces in Chapter 3 and 3D generalization in Chapter 6 provide first steps towards three important features needed in future designs. Another important research direction is the use of an acoustic hyperlens as a sub-diffraction limit focusing device for high intensity focused ultrasound or naval applications, which has attracted the interest of industry.

The negative acoustic index work presented in Chapters 4 and 5 indicates much more basic research remains to be done in the development of useful negative acoustic index metamaterials. It may be that RS resonators cannot create negative density with realistic amounts of intrinsic loss, with coupled resonators and specially designed loss tolerant resonators identified as two new methods for future research. It is likely though that active acoustic metamaterials will be necessary to truly advance negative acoustic index metamaterial research. Currently in its infancy and limited simple studies, active elements provide the ultimate solution to loss and bandwidth issues, and also have many potential new capabilities and applications such as energy trapping and releasing, non-linear effects, and cloaking. Much engineering and scientific work remains to be done to advance active acoustic metamaterials.

References

1. D. R. Smith, W. J. Padilla, D. C. Vier, S. C. Nemat-Nasser, and S. Schultz, Composite medium with simultaneously negative permeability and permittivity. *Phys. Rev. Lett.* 84 (18), 4184 (2000)
2. D. Griffiths, Introduction to Electrodynamics, 3rd Ed. Prentice Hall, ©1999
3. D. Schurig, J. J. Mock, B. J. Justice, S. A. Cummer, J. B. Pendry, A. F. Starr, and D. R. Smith, Metamaterial electromagnetic cloak at microwave frequencies. *Science* 314, 977 (2006)
4. A. Ishikawa, S. Zhang, D. A. Genov, G. Bartal, and X. Zhang, Deep subwavelength terahertz waveguides using gap magnetic plasmon. *Phys. Rev. Lett.* 102, 043904 (2009)
5. G. W. Milton and J.R. Willis, On modifications of Newton's second law and linear continuum elastodynamics. *Proc. R. Soc. A* 463, 855 (2007)
6. L. E. Kinsler, A. R. Frey, A. B. Coppers, and J. V. Sanders, Fundamentals of Acoustics, 4th Ed. John Wiley & Sons ©2000
7. B. B. Goldberg, J.-B. Liu, and F. Forsberg, Ultrasound contrast agents: a review. *Ultrasound in Med. & Bio.* 20 (4), 319 (1994)
8. J. P. Watt, G. F. Davies, and R. J. O'Connell, The elastic properties of composite materials. *Rev. Geophys. and Space Phys.* 14 (4), 541 (1976)
9. J. G. Berryman, Theory of elastic properties of composite materials. *Appl. Phys. Lett.* 35 (11), 856 (1979)
10. A. K. Mal and L. Knopoff, Elastic wave velocities in two-component systems. *J. Inst. Maths. Applics.* 3 (4), 376 (1966)
11. J. G. Berryman, Long-wavelength propagation in composite elastic media I. Spherical inclusions. *J. Acou. Soc. Am.* 68 (6), 1809 (1980)
12. J. G. Berryman, Long-wavelength propagation in composite elastic media II. ellipsoidal inclusions. *J. Acou. Soc. Am.* 68 (6), 1820 (1980)
13. P. Sheng, J. Mei, Z. Liu, and W. Wen, Dynamic mass density and acoustic metamaterials. *Physica B* 394, 256 (2007)
14. Z. Liu, X. Zhang, Y. Mao, Y. Y. Zhu, Z. Yang, C. T. Chan, and P. Sheng, Locally resonant sonic materials. *Science* 289, 1734 (2000)
15. V. Fokin, M. Ambati, C. Sun, and X. Zhang, Method for retrieving effective properties of locally resonant acoustic metamaterials. *Phys. Rev. B* 76, 144302 (2007)

16. M. S. Kushwaha, P. Halevi, G. Martinez, L. Dobrzynski, and B. Djafari-Rouhani, Theory of acoustic band structure of periodic elastic composites. *Phys. Rev. B* 49 (4), 2313 (1994)
17. C. Rubio, D. Caballero, J. V. Sánchez-Pérez, R. Martínez-Sala, J. Sánchez-Dehesa, F. Meseguer, and F. Cervera, The existence of full gaps and deaf bands in two-dimensional sonic crystals. *J. Lightwave Tech.* 17 (11), 2202 (1999)
18. S. Yang, J. H. Page, Z. Liu, M. L. Cowan, C. T. Chan, and P. Sheng, Ultrasound tunneling through 3D phononic crystals. *Phys. Rev. Lett.* 88 (10), 104301 (2002)
19. Z. Liu, C. T. Chan, and P. Sheng, Three-component elastic wave band-gap material. *Phys. Rev. B* 65, 165116 (2002)
20. C. Luo, S. G. Johnson, J. D. Joannopoulos, and J. B. Pendry, All-angle negative refraction without negative effective index. *Phys. Rev. B* 65, 201104 (2002)
21. X. Zhang and Z. Liu, Negative refraction of acoustic waves in two-dimensional phononic crystals. *Appl. Phys. Lett.* 85 (2), 341 (2004)
22. S. Yang, J. H. Page, Z. Liu, M. L. Cowan, C. T. Chan, and P. Sheng, Focusing of sound in a 3D phononic crystal. *Phys. Rev. Lett.* 93 (2), 024301 (2004)
23. C. Qui, X. Zhang, and Z. Liu, Far-field imaging of acoustic waves by a two-dimensional sonic crystal. *Phys. Rev. B* 71, 054302 (2005)
24. L. Feng, X. Liu, Y. Chen, Z. Huang, Y. Mao, Y. Chen, J. Zi, and Y. Zhu, Negative refraction of acoustic waves in two-dimensional sonic crystals. *Phys. Rev. B* 72, 033108 (2005)
25. L. Feng, X. Liu, M. Lu, Y. Chen, Y. Chen, Y. Mao, J. Zi, Y. Zhu, S. Zhu, and N. Ming, Refraction control of acoustic waves in a square-rod-constructed tunable sonic crystal. *Phys. Rev. B* 73, 193101 (2006)
26. A. Bazan, M. Torres, F. R. Montero de Espinosa, R. Quintero-Torres, and J. L. Aragon, Conformal mapping of ultrasonic crystals: Confining ultrasound and cochlearlike waveguiding. *Appl. Phys. Lett.* 90, 094101 (2007)
27. L. Wu, W. Yang, and L. Chen, The thermal effects on the negative refraction of sonic crystals. *Phys. Lett. A* 372, 2701 (2008)
28. C. Kittel, Introduction to Solid State Physics. 8th ed. Wiley, ©2005
29. J. Li, L. Fok, X. Yin, G. Bartel, and X. Zhang, Experimental demonstration of an acoustic magnifying hyperlens. *Nat. Matl.* 8, 931 (2009)
30. D. A. Genov, S. Zhang, and X. Zhang, Mimicking celestial mechanics in metamaterials. *Nat. Phys.* 5, 687 (2009)

31. D. Schurig, J. J. Mock, B. J. Justice, S. A. Cummer, J. B. Pendry, A. F. Starr, and D. R. Smith, Metamaterial electromagnetic cloak at microwave frequencies. *Science* 314, 977 (2006)
32. G. W. Milton, M. Briane, and J.R. Willis, On cloaking for elasticity and physical equations with a transformation invariant form. *New J. Phys.* 8, 248 (2006)
33. S. A. Cummer and D. Schurig, One path to acoustic cloaking. *New J. Phys.* 9, 45 (2007)
34. A. Salandrino and N. Engheta, Far-field subdiffraction optical microscopy using metamaterial crystals: theory and simulations. *Phys. Rev. B* 74, 075103 (2006)
35. Z. Jacob, L. V. Alekseyev, and E. Narimanov, Optical hyperlens: far-field imaging beyond the diffraction limit. *Opt. Exp.* 14 (18), 8247 (2006)
36. Z. Liu, H. Lee, Y. Xiong, C. Sun, and X. Zhang, Far-field optical hyperlens magnifying sub-diffraction-limited objects. *Science* 315, 1686 (2007)
37. D. Torrent & J. Sánchez-Dehesa, Anisotropic mass density by two-dimensional acoustic metamaterials. *New J. Phys.* 10, 023004 (2008)
38. X. Ao and C.T. Chan, Far-field image magnification for acoustic waves using anisotropic acoustic metamaterials. *Phys. Rev. E* 77, 025601 (2008)
39. M. Kafesaki and E. N. Economou, Multiple-scattering theory for three-dimensional periodic acoustic composites. *Phys. Rev. B.* 60, 11993 (1999)
40. L.M. Brekhovskikh, Waves in Layered Media, Academic Press, 1980
41. S. Han, Y. Xiong, D. Genov, Z. Liu, G. Bartel, and X. Zhang, Ray optics at deep-subwavelength scale: a transformation optics approach. *Nano Lett.* 8 (12), 4243 (2008)
42. S. Choi and Y. Kim, Sound-wave propagation in a membrane-duct (L). *J. Acoust. Soc. Am.* 112 (5), 1749 (2002)
43. Y. H. Chiu, L. Cheng, and L. Huang, Drum-like silencers using magnetic forces in a pressurized cavity. *J. Sound and Vib.* 297, 895 (2006) (2 May 2006)
44. V. G. Veselago, The electrodynamics of substances with simultaneously negative values of ϵ and μ . *Soviet Physics Uspekhi* 10 (4), 509 (1968)
45. M. Ambati, N. Fang, C. Sun, and X. Zhang, Surface resonant states and superlensing in acoustic metamaterials. *Phys. Rev. B* 75, 195447 (2007)
46. J. B. Pendry, Negative refraction makes a perfect lens. *Phys. Rev. Lett.* 85 (18), 3966 (2000)

47. N. Garcia and M. Nieto-Vesperinas, Left-handed materials do not make a perfect lens. *Phys. Rev. Lett.* 88 (20), 207403 (2002)
48. N. Fang, H. Lee, C. Sun, and X. Zhang, Sub-diffraction-limited optical imaging with a silver superlens. *Science* 308, 534 (2005) (22 Apr 2005)
49. X. Hu, C. T. Chan, and J. Zi, Two-dimensional sonic crystal with Helmholtz resonators. *Phys. Rev. E* 71, 055601 (2005)
50. N. Fang, D. Xi, J. Xu, M. Ambati, W. Srituravanich, C. Sun, and X. Zhang, Ultrasonic metamaterials with negative modulus. *Nat. Matl.* 5, 452 (2006)
51. S. H. Lee, C. M. Park, Y. M. Seo, Z. G. Wang, and C. K. Kim, Acoustic metamaterial with negative modulus. *J. Phys.: Condens. Matter* 21, 175704 (2009)
52. Z. Liu, C. T. Chan, and P. Sheng, Analytic model of phononic crystals with local resonances. *Phys. Rev. B* 71, 014103 (2005)
53. J. Mei, Z. Liu, W. Wen, and P. Sheng, Effective mass density of fluid-solid composites, *Phys. Rev. Lett.* 96, 024301 (2006)
54. Z. Yang, J. Mei, M. Yang, N.H. Chan, and P. Sheng, Membrane-type acoustic metamaterial with negative dynamic mass. *Phys. Rev. Lett.* 101, 204301 (2008)
55. S. H. Lee, C. M. Park, Y. M. Seo, Z. G. Wang, and C. K. Kim, Acoustic metamaterial with negative density. *Phys. Lett. A* 373, 4464 (2009)
56. J. Li and C.T. Chan, Double-negative acoustic metamaterial. *Phys. Rev. E* 70, 055602 (2004)
57. J. Li, Z. Liu, and C. Qiu, Negative refraction imaging of acoustic waves by a two-dimensional three-component phononic crystal. *Phys. Rev. B* 73, 054302 (2006)
58. Y. Ding, Z. Liu, C. Qiu, and J. Shi, Metamaterial with simultaneously negative bulk modulus and mass density. *Phys. Rev. Lett.* 99, 093904 (2007)
59. Y. Cheng, J. Y. Xu, and X. J. Liu, One-dimensional structured ultrasonic metamaterials with simultaneously negative dynamic density and modulus. *Phys. Rev. B* 77, 045134 (2008)
60. K. Deng, Y. Ding, Z. He, H. Zhao, J. Shi, and Z. Liu, Theoretical study of subwavelength imaging by acoustic metamaterial slabs. *J. App. Phys.* 105, 124909 (2009)
61. S. Zhang, L. Yin, and N. Fang, Focusing ultrasound with an acoustic metamaterial network. *Phys. Rev. Lett.* 102, 194301 (2009)

62. S. H. Lee, C. M. Park, Y. M. Seo, Z. G. Wang, and C. K. Kim, Composite acoustic medium with simultaneously negative density and modulus. *Phys. Rev. Lett.* 104, 054301 (2010)
63. J. D. Jackson, Classical Electrodynamics, 3rd Ed. Wiley, ©1999
64. L. Fok, M. Ambati, and X. Zhang, Acoustic Metamaterials. *MRS Bulletin* 33, 931 (2008)
65. S. Mousavi, D. F. Nicolas, and B. Lundberg, Identification of complex moduli and Poisson's ratio from measured strains on an impacted bar. *J. Sound and Vib.* 277, 971 (2004)
66. Y. Liao and V. Wells, Estimation of complex modulus using wave coefficients. *J. Sound and Vib.* 295, 165 (2006)
67. V. M. Shalaev, W. Cai, U. K. Chettiar, H. Yuan, A. K. Sharychev, V. P. Drachev, and A. V. Kildishev, Negative index of refraction in optical metamaterials. *Opt. Lett.* 30 (24), 3356 (2005) (14 Oct 2005)
68. J. Valentine, S. Zhang, T. Zentgraf, E. Ulin-Avila, D. A. Genov, G. Bartel, and X. Zhang, Three-dimensional optical metamaterial with a negative refractive index. *Nature* 455, 376 (2008)
69. M. Ambati, S. H. Nam, E. Ulin-Avila, D. A. Genov, G. Bartel, and X. Zhang, Observation of stimulated emission of surface plasmon polaritons. *Nano Letters* 8, 3998 (2008)
70. P. M. Walker, A. J. Kent, M. Henini, B. A. Glavin, V. A. Kochelap, and T. L. Linnik, Terahertz acoustic oscillations by stimulated phonon emission in an optically pumped superlattice. *Phys. Rev. B* 79, 245313 (2009)
71. A. Baz, The structure of an active acoustic metamaterial with tunable effective density. *New J. Phys.* 11, 123010 (2009)
72. W. Akl and A. Baz, Multi-cell active acoustic metamaterial with programmable bulk modulus. *J. Intel. Mat. Sys. Struct.* 21, 541 (2010)
73. W. Akl and A. Baz, Configurations of active acoustic metamaterial with programmable bulk modulus. *Proc. SPIE* 7643, 76432K (2010)